REVISITING THE STATISTICAL RELATIONSHIP BETWEEN SOLAR ACTIVITY AND ASIAN MONSOON DURING THE HOLOCENE

Yue Zhang

A thesis submitted to the faculty of the University of North Carolina at Chapel Hill in partial fulfillment of the requirements for the degree of Master of Science in the Department of Geological Sciences (Geophysics).

Chapel Hill
2012

Approved by:

Donna M. Surge

John M. Bane

Jonathan M. Lees

ABSTRACT

YUE ZHANG: REVISITING THE STATISTICAL RELATIONSHIP BETWEEN SOLAR ACTIVITY AND ASIAN MONSOON DURING THE HOLOCENE
(Under the direction of Donna M. Surge)

The relationship between the sun and terrestrial climate in the past has been controversial. Given the difficulty in understanding the underlying mechanism(s) of solar influence on the climate system, the empirical relationship between the sun and climate variables relies on statistical analyses. The tight link between proxies for solar irradiance and the Asian monsoon has gained wide consensus; however, this unresolved scientific issue is still under debate. Here, the nonlinear and nonstationary relationship between solar activity and Asian monsoon strength during the last 8,800 years is investigated with Ensemble Empirical Mode Decomposition (EEMD) and Wavelet Coherence (WTC). The results show the coherence between solar activity and Asian monsoon strength is low in time-frequency-oscillatory mode representation. There is no causal relationship between solar activity and Asian monsoon strength during the Holocene that can be identified. This research provides a new insight into the sun-Asian monsoon interaction.

To my grandfather and my uncle

ACKNOWLEDGEMENTS

I would never have been able to finish my thesis without the guidance of my committee members. Foremost, I would like to express my sincere gratitude to my advisor Dr. Donna Surge for the continuous support, advice and encouragement throughout my research. One simply could not wish for a better or friendlier advisor. Second, I would like to thank the rest of my committee members, Dr. John Bane and Dr. Jonathan Lees, for their insightful comments and encouragement. I sincerely appreciate their patience to answer my questions when I attended their Geophysical Fluid Dynamics and Data Analysis in the Earth Sciences classes.

Moreover, I would like to show my sincere thanks to Deborah Harris and Elizabeth Mullane for their help to make the department run smoothly and for their assistance in many different ways. I am also grateful to Dr. Allen Glazner, Dr. Leslie Lerea and Anne Schwarz for their strong support in my hard time.

Besides, I would like to thank my colleague Ting Wang for her help and encouragement in many aspects. It is a great pleasure to share an office with her. Also, thank all fellow students in UNC geology. It is an honor to enjoy two-year indelible time with you all in this great university.

In addition, I would like to thank Ambrose Chiang, David Stickel, Yan Wang and Jun Xiong for their help in my living. Thank all my friends and people who gave me help. For them, I don’t feel lonely.

Lastly and most importantly, I wish to thank my family: my parents, who gave me life and love me forever.

TABLE OF CONTENTS

LIST OF TABLES

Table

LIST OF FIGURES

Figure

LIST OF ABBREVIATIONS

AD	Anno Domini
AR1	first-order autoregressive
BP	Before Present
COI	Cone of Influence
CWT	Continuous Wavelet Transform
EMD	Empirical Mode Decomposition
EEMD	Ensemble Empirical Mode Decomposition
et al.	et alia
etc	et cetera
GRIP	Greenland Ice Core Project
i.e.	id est
IMF	Intrinsic Mode Function
kyr	kiloyear
pm	post meridiem
WTC	Wavelet Coherence
yr	year

LIST OF SYMBOLS

^{10}Be	beryllium isotope 10
^{14}C	radiocarbon isotope 14
^{13}C	carbon isotope 13
^{12}C	carbon isotope 12
$\Delta^{14}C$	ratio of ^{14}C to ^{12}C
CO_2	carbon dioxide
DA	a stalagmite sample from Dongge Cave
^{14}N	nitrogen isotope 14
^{18}O	oxygen isotope 18
^{16}O	oxygen isotope 16
$\delta^{18}O$	delta notation of the ^{18}O:^{16}O ratio of a sample relative to a standard
^{230}Th	thorium isotope 230
∞	infinity

Revisiting the statistical relationship between solar activity and Asian monsoon during the Holocene[1]

Abstract

The relationship between the sun and terrestrial climate in the past has been controversial. Given the difficulty in understanding the underlying mechanism(s) of solar influence on the climate system, the empirical relationship between the sun and climate variables relies on statistical analyses. The tight link between proxies for solar irradiance and the Asian monsoon has gained wide consensus; however, this unresolved scientific issue is still under debate. Here, the nonlinear and nonstationary relationship between solar activity and Asian monsoon strength during the last 8,800 years is investigated with Ensemble Empirical Mode Decomposition (EEMD) and Wavelet Coherence (WTC). The results show the coherence between solar activity and Asian monsoon strength is low in time-frequency-oscillatory mode representation. There is no causal relationship between solar activity and Asian monsoon strength during the Holocene that can be identified. This research provides a new insight into the sun-Asian monsoon interaction.

[1]It is a non-published work to be submitted to *Climate of the Past*. The authors are Y. Zhang (corresponding author), D. Surge, J. M. Lees, and J. M. Bane.

Introduction

The Earth's climate is controlled by external forcings and internal processes. As the heat engine of the Earth's climate system, the sun is the most dominant external forcing and is considered to affect climate variability in the past, present and future (Beer et al., 2000; Crowley, 2000; Bond et al., 2001; Haigh, 2001; Shindell et al., 2001; Rind, 2002; Gimeno et al., 2003; Braun et al., 2005). Accurate reconstruction of past climate change is critical to projecting future climate changes (Gray et al., 2010). Thus, characterizing the contribution of solar activity to climate variability over disparate timescales has been a focus of study for the last several decades. However, long-term observation of solar activity is sparse. Telescopic observations of sunspot numbers extend from the present back to AD 1610, while satellite monitoring of total solar irradiance only began in 1978 (Solanki et al., 2004). Reconstructing the variation of solar activity over geological timescales (in particular, during the Holocene) relies on proxy records of solar activity, such as various cosmogenic radionuclides (e.g., ^{10}Be and ^{14}C). Similarly, climate variability that occurred before the era of instrumental observation is typically reconstructed using proxy records such as ice cores, tree rings, marine sediments, speleothems, archaeological and fossil shells, etc. Hence, dynamical links between solar activity and past climate variability are often proposed based on the statistical relationships between proxies for solar activity and those for past climate change (Legras et al., 2010; Yiou et al., 2010).

The Asian monsoon is a subsystem of the climate system which modulates large-scale variations between the ocean and the continents. Billions of people live in Asia, and local agriculture, water resources and economic activity there are all influenced by Asian monsoon

precipitation. Given its practical implications for climate change and population, an understanding of the Asian monsoon system, especially the ability to better predict Asian monsoon variations from annual to decadal and longer, is imperative. Understanding the Asian monsoon system is intricately linked to knowledge about past changes of the Asian monsoon and the influence of natural forcings on Asian monsoon variations in the past. Motivated by this, many studies have focused on the interaction between solar activity and Asian monsoon strength during the Holocene. Neff et al. (2001) studied the coherence between atmospheric $\Delta^{14}C$ (the ratio of radiocarbon ^{14}C to ^{12}C in the atmosphere) and $\delta^{18}O$ (the ratio of ^{18}O to ^{16}O) values from a speleothem in Hoti Cave, northern Oman, that accumulated in the early Holocene. They suggested that decadal to centennial variability of rainfall and monsoon strength in the early Holocene was dominated by solar activity. Fleitmann et al. (2003) measured the correlation between atmospheric $\Delta^{14}C$ and speleothem $\delta^{18}O$ values from Qunf Cave, southern Oman, and reported that decadal to multi-decadal variations of monsoonal precipitation were controlled by solar activity after 8 kyr BP (before present, 0 year BP = AD 1950). Wang et al. (2005) estimated the link between atmospheric $\Delta^{14}C$ and $\delta^{18}O$ values from a Dongge Cave speleothem in southern China. They indicated that decadal to centennial variability of monsoon strength during the Holocene partly resulted from changes in solar radiation. According to the previous studies, the sun-Asian monsoon interaction has gained widespread acceptance (Wang et al., 1999; Hong et al., 2001; Neff et al., 2001; Agnihotri et al., 2002; Fleitmann et al., 2003; Staubwasser et al., 2003; Higginson et al., 2004; Clemens, 2005; Gupta et al., 2005; Wang et al., 2005; Xiao et al., 2006; Zhang et al., 2008; Cai et al., 2010). However, a careful scrutiny of the analyses in these studies calls this consensus into question.

The accumulation of ^{14}C in the atmosphere results from the interaction between cosmic rays and atmospheric ^{14}N. When solar activity strengthens, cosmic rays reaching the atmosphere are reduced and it further decreases ^{14}C production (Gray et al., 2010). Hence, atmospheric $\Delta^{14}C$ is generally regarded as an indicator of solar activity. However, solar activity is not the sole factor controlling the production of atmospheric $\Delta^{14}C$. Cosmic rays mainly consist of charged particles. When cosmic rays penetrate the atmosphere, the geomagnetic field deflects a large portion of cosmic rays. Therefore, variation of the geomagnetic field intensity is a major factor that can modulate the ^{14}C production rate (Mazaud et al., 1991; Hughen et al., 2004). Once ^{14}C is produced in the atmosphere, it is transported to other exchangeable carbon reservoirs through the global carbon cycle (Muscheler et al., 2007; Burke and Robinson, 2012). The ocean has substantial storage capacity of CO_2 and it is the most important one of these reservoirs. Radiocarbon can be captured by ocean water through air-sea exchange of CO_2. Because of the limited ventilation of the abyssal ocean, the carbon-enriched water in the deep ocean can be isolated from the atmosphere (Muscheler et al., 2000; Marchitto et al., 2007). Some isolated carbon in the abyssal ocean is too old to contain detectable ^{14}C as a result of radioactive decay. Nevertheless, once deep water upwells because of reinitiated ventilation and a reorganized meridional overturning circulation, CO_2 with low ^{14}C that had been sequestrated in the deep ocean can be released into the atmosphere. Consequently, the atmospheric ^{14}C inventory can be regulated by processes in addition to solar activity (Stocker and Wright, 1996; Rose et al., 2010; Skinner et al., 2010). Because the annual production by both solar activity and geomagnetic field effect is relatively small in contrast to the global ^{14}C inventory, the

influence of the carbon cycle on ^{14}C variation can overcome the effect of solar activity (Bradley, 1999). Moreover, the terrestrial biosphere plays a key role in the global carbon cycle (Hahn and Buchmann, 2004; Naegler and Levin, 2009). Radiocarbon in fossil fuel is low owing to radioactive decay. Burning of fossil fuel makes ^{13}C and ^{12}C become more enriched in the atmosphere. Accordingly, human use of fossil fuel can also greatly reduce $\Delta^{14}C$ over the globe (Suess, 1955). Hence, atmospheric $\Delta^{14}C$ is dominated by both ^{14}C production rate, and climate-related, and human-induced processes (Kitagawa and van der Plicht, 1998). It is not a pure proxy for solar activity in the past.

As a proxy for Asian monsoon activity, $\delta^{18}O$ values from speleothem records reflect stable isotopic variations in local precipitation. These values characterize precipitation amount and, hence, Asian monsoon strength (Yuan et al., 2004; Dykoski et al., 2005; Wang et al., 2005). However, $\delta^{18}O$ values in speleothems are also dominated by cave conditions (e.g., temperature and humidity), deposition processes, and the hydrological cycle. Speleothem carbonate is mainly precipitated from percolated groundwater, and formation largely relies on water evaporation and CO_2 degassing associated with temperature and humidity in the cave (Bradley, 1999). The deposition process can be affected by factors which can modulate groundwater percolation or speleothem growth (Bradley, 1999). In addition, the percolated water in the cave is typically a mixture of groundwater, meteoric water, soil water, plant water and surface water. Thus, the isotopic composition of a cave water droplet does not merely reflect the $\delta^{18}O$ values of local precipitation. Measurements of the isotopic composition of precipitation in Asia reflect a complex spatio-temporal pattern, which results from heterogeneous air masses and moisture sources in this region and the

consecutive fractionation processes at water phase transitions (i.e., condensation and evaporation) in the hydrological cycle (Araguas-Araguas et al., 1998; Jouzel et al., 2000; Johnson and Ingram, 2004). Therefore, $\delta^{18}O$ values recorded in speleothems represent several factors rather than simply Asian monsoon strength (Lachniet, 2009). In summary, both $\Delta^{14}C$ and $\delta^{18}O_{speleothem}$ values are composite signals, as opposed to pure indicators of climate variables. Accordingly, the direct comparison between two complicated signals may not clearly reveal the underlying mechanisms of solar influence on the Asian monsoon.

Several studies have reported a strong correspondence between atmospheric $\Delta^{14}C$ and $\delta^{18}O_{speleothem}$ values (Neff et al., 2001; Fleitmann et al., 2003; Wang et al., 2005). However, this correspondence is suspect because a phase shift should exist between them if they clearly represent solar activity and monsoon strength respectively, and $\Delta^{14}C$ should lead $\delta^{18}O_{speleothem}$. The different components of the climate system have distinct response time to external forcing (IPCC, 2007). Modern observations show a lead-lag relation between solar irradiance and temperature. Solar irradiance is a flux of energy, while temperature is an index of the divergence of this flux. If the energy flux varies with some period, its time derivative has a phase shift. The daily maximum of solar irradiance occurs around noon, for example, while the daily maximum temperature occurs at about 3 pm. Moreover, the seasonal maximum of Northern Hemisphere solar irradiance occurs in late June, while the seasonal maximum temperature occurs at the end of July or in early August. If solar irradiance is close to a sinusoidal function, the phase change between solar irradiance and temperature is approximately 1/8 of the period (45 degrees), which is 3 hours for the diurnal cycle or 1.5 months for the annual cycle (A. Ohmura, personal communication, 2011). In addition,

insolation variability caused by long-term changes in Earth's orbital parameters leads the marine $\delta^{18}O$ record (indicating ice volume variations) by 90 degrees on orbital time scales, which is 10,000 years for obliquity band and 6,000 years for precession band (Ruddiman, 2007). As a weather system, the Asian monsoon's response to variation of solar irradiance is much slower than that of temperature and much faster than that of ice sheets because of a series of complex physical processes and feedbacks. Hence, the phase angle between solar activity and Asian monsoon is expected to be between 45 and 90 degrees. Moreover, $\Delta^{14}C$ should not be in phase with $\delta^{18}O_{speleothem}$ values, but rather should lead it. A strong correspondence may be unreasonable to expect.

Haam and Huybers (2010) measured the linear and in-phase covariance between atmospheric $\Delta^{14}C$ and stalagmite DA $\delta^{18}O$ from Dongge Cave with a novel methodology for maximum covariance test of time-uncertain series. They suggested that the correlation coefficient of 0.3 between solar activity and Asian monsoon strength reported by Wang et al. (2005) is insignificant at the 95% confidence level. This implies that there might be no causal relationship between solar activity and Asian monsoon strength during the Holocene. However, a nonlinear and nonstationary link between solar activity and Asian monsoon strength cannot be ruled out based solely on their analysis.

Inspired by these two problems and the contradictory conclusion by Haam and Huybers (2010), it is necessary to quantitatively test the nonlinear and nonstationary relationship between solar activity and Asian monsoon strength during the Holocene using other statistical methods. This should provide new understanding about the mechanism of

solar influence on the Asian monsoon. The proxy records for both solar irradiance and the Asian monsoon ($\Delta^{14}C$ and $\delta^{18}O_{speleothem}$) are composite signals superimposed by various underlying processes in the climate system. As proxy records, it is assumed that $\Delta^{14}C$ and $\delta^{18}O_{speleothem}$ time series contain information of past solar and Asian monsoon activity. If the Asian monsoon is paced unidirectionally by the sun during the Holocene, the sun should leave a signature in both the $\Delta^{14}C$ and $\delta^{18}O_{speleothem}$ records. $\Delta^{14}C$ and $\delta^{18}O_{speleothem}$ time series should contain similar underlying processes with similar periods and appropriate phase relations. Following this rationale, time series for atmospheric $\Delta^{14}C$, total solar irradiance (reconstructed from ^{10}Be accumulated in ice cores), and $\delta^{18}O_{speleothem}$ are decomposed into inherent components using Ensemble Empirical Mode Decomposition (EEMD), a newly applied procedure in paleoclimatology. Wavelet Coherence (WTC) is then employed to quantify the coherence and phase relationship between the corresponding processes from the EEMD results.

Data and methods

Data

Previously documented records of atmospheric $\Delta^{14}C$, total solar irradiance, and $\delta^{18}O_{speleothem}$ are used in this study (Figures 1-3). The atmospheric $\Delta^{14}C$ time series was reconstructed with a synthesized sample of tree rings, corals and marine sediments from all over the globe (Stuiver et al., 1998). There is an empirical relationship between total solar irradiance and the open solar magnetic field. Steinhilber et al. (2008) reconstructed the open solar magnetic field using the ^{10}Be record in ice cores from GRIP, Dye 3 and the South Pole,

which is also dominated by solar activity. Total solar irradiance was computed based upon its functional relation with the open solar magnetic field (Steinhilber et al., 2009). A stalagmite DA was retrieved from Dongge Cave (25°17′N, 108°5′E, elevation 680m) in south China (Wang et al., 2005). The corresponding $\delta^{18}O$ record is dominated by isotopic variations in local meteoric water, which is further related to variations in precipitation amount characterizing Asian monsoon strength. The chronology of the Dongge Cave stalagmite was constructed using ^{230}Th dating, and the typical age uncertainty is about 50 years. The time span of all records is from 8,800 year BP to 0 year BP. All the data linearly interpolated with a 10-year sampling interval.

Ensemble empirical mode decomposition (EEMD)

EEMD and WTC are used to analyze the time series. Empirical Mode Decomposition (EMD) is an adaptive data decomposition method with an a posteriori basis, which implicitly assumes the data is a superposition of several simple oscillatory components with significantly different frequencies (Huang, 2005; Huang and Wu, 2008). Each simple oscillatory component must satisfy two conditions. First, the number of extrema and the number of zero-crossings must be the same or do not differ more than one in the whole dataset. Second, the mean of the two envelopes, which are respectively represented by the local maxima and minima, must be zero at any point. Such a component is called an Intrinsic Mode Function (IMF), and it represents a physically meaningful underlying process in the data. With a sifting process, any complicated dataset can be decomposed into a series of IMFs from higher frequency to lower frequency, and a residue. Take signal $x(t)$ as an example. After the identification of all the local extrema, all the local maxima and minima

are connected respectively by two cubic spline curves to generate the upper and lower envelopes, where m_1 is the mean of the two envelopes and h_1 is the first component that equals the difference between $x(t)$ and m_1.

$$h_1 = x(t) - m_1$$

However, the new extrema may be generated as a result of changing the local zero from a rectangular coordinate system to a curvilinear one. Hence, h_1 needs to be sifted repeatedly to eliminate the riding waves (background signals) and make the time series more symmetric.

$$h_1 - m_2 = h_2$$

After k times of sifting,

$$h_{k-1} - m_k = h_k$$

The first IMF c_1 is obtained

$$c_1 = h_k$$

The number of iterations, k, is determined by stoppage criteria (Huang, 2005). A typical stoppage criterion is a Cauchy type of convergence test that requires the normalized squared difference between two successive sifting processes:

$$SD_k = \frac{\sum_{t=0}^{T} |h_{k-1}(t) - h_k(t)|^2}{\sum_{t=0}^{T} h_{k-1}^2(t)}$$

to be smaller than a predetermined value. Once it satisfies this stoppage condition, the sifting ends. After satisfying the stoppage condition, the first IMF c_1, the oscillatory component with the highest frequency, is obtained. Then, a residue r_1 can be obtained by removing the first IMF c_1 from the original data.

$$x(t) - c_1 = r_1$$

Because r_1 still contains oscillatory modes with lower frequencies, the sifting process can be employed again after considering r_1 as a new time series.

$$r_1 - c_2 = r_2$$

This is repeated until the sifting process is stopped when no IMF can be extracted from the residue r_n.

$$r_{n-1} - c_n = r_n$$

Therefore, the original data can be represented with n IMFs and a residue r_n.

$$x(t) = \sum_{j=1}^{n} c_j + r_n$$

The final residue can be considered to be a trend. Because the decomposition directly works in the temporal domain but not in the frequency domain and only relies on the local characteristics of the data, EMD can solve the nonlinearity and nonstationarity of the data. However, the EMD-produced results may have a mode-mixing problem, which is caused by signal intermittency (Huang and Wu, 2008).

An IMF either contains signals with widely different scales or a signal with similar scale is distributed in different IMFs. To overcome this drawback, a white noise-assisted decomposition method, EEMD, was developed (Wu and Huang, 2005). After introducing a uniform background of white noise, the true signals can distribute in correct scales. In this new approach, white noise is added to the original data, and the noisy data is decomposed

with EMD first. Then, this procedure is repeated with distinct white noise time series. The final result in EEMD is defined as the ensemble mean of all corresponding EMD-produced IMFs. Though each time's result is very noisy, the noise can be canceled out with averaging. Nevertheless, the EEMD results do not strictly satisfy the two conditions for IMF. Hence, one more sifting is done to eliminate the riding wave (Huang and Wu, 2008).

Wavelet coherence (WTC)

Wavelet analysis uses a zero-mean wavelet to fit a time series in both time and frequency domains (Grinsted et al., 2004). As a locally periodic wavetrain, the Morlet, a Gaussian-windowed complex sinusoid, is expressed as:

$$\psi_0(\eta) = \pi^{-1/4} e^{i\omega_0 \eta} e^{-\frac{1}{2}\eta^2}$$

where η and ω_0 are dimensionless time and frequency, respectively. Continuous Wavelet Transform (CWT) is defined as:

$$W_n^X(s) = \sqrt{\frac{\delta t}{s}} \sum_{n'=1}^{N} x_{n'} \, \psi_0 \left[(n' - n) \frac{\delta t}{s} \right]$$

This can be seen as a convolution of a time series with a scaled and normalized wavelet, where $|W_n^X(s)|^2$ and the complex argument of $W_n^X(s)$ represent wavelet power and local phase, respectively. Wavelet Coherence (WTC) measures the coherence and phase relationships between two time series and is defined as:

$$R_n^2(s) = \frac{\left| S\left(s^{-1} W_n^{XY}(s)\right) \right|^2}{S(s^{-1}|W_n^X(s)|^2) \cdot S(s^{-1}|W_n^Y(s)|^2)}$$

where S, a smoothing operator, defined as:

$$S(W) = S_{scale}\left(S_{time}\left(W_n(s)\right)\right)$$

where S_{scale} and S_{time} are the smoothing in Wavelet scale and in time. For the Morlet, the smoothing operator is defined as:

$$S_{time}(W)|_s = \left(W_n(s) * c_1^{\frac{-t^2}{2s^2}}\right)\Big|_s$$

$$S_{time}(W)|_s = \left(W_n(s) * c_2 \prod(0.6s)\right)\Big|_n$$

where c_1 and c_2 are normalization constants, and $\prod$ is a rectangle function (Torrence and Webster, 1998). The value 0.6 is a scale decorrelation length, which is decided empirically for the Morlet (Torrence and Compo, 1998).

Due to the non-localization of a wavelet in time domain, a Cone of Influence (COI) is introduced in the result to consider the edge effects. The significane level for WTC is computed with the Monte Carlo method. The coherence of each of 1000 surrogate data set pairs with the same AR1 coefficients is measured. Afterward, the significance level for each scale is computed based on the values outside the COI only (Grinsted et al., 2004). Before analyzing the paleoclimate data in this study, WTC was tested with a series of synthesized time series to check the validity of the resulting coherence and phase angles. The result of this test demonstrates WTC can capture the detailed common power and local phase relation between two time series.

Significance test

Proxy records are generally contaminated by noise. A significance test of the IMFs is necessary to estimate whether an IMF represents the true signal or only consists of noise. Wu and Huang (2004) developed a test of statistical significance based on the characteristics of white noise and the orthogonality of the IMFs. For normalized white noise, f_j, the energy density of the *n*th IMF $C_n(j)$ can be expressed as:

$$E_n = \frac{1}{N}\sum_{j=1}^{N}[C_n(j)]^2$$

The total energy is defined as:

$$\sum_{n=1}^{N} {f_j}^2 = \sum_{k=1}^{N}|F_k|^2 = N\sum_{n} E_n$$

where $i = \sqrt{-1}$, f_j and F_k are respectively represented as:

$$f_j = Re\left[\sum_{k=1}^{N} F_k e^{i\frac{2\pi jk}{N}}\right] = \sum_{n} C_n(j)$$

and

$$F_k = \sum_{j=1}^{N} f_j e^{-i\frac{2\pi jk}{N}}$$

Consequently, it is suggested that the energy density of an IMF and its average period satisfy a hyperbolic relationship:

$$\ln\overline{E_n} + \ln\overline{T_n} = 0$$

where $\overline{E_n}$ equals the mean of E_n if n $\rightarrow \infty$. If an IMF's energy density is located above the upper spread lines of the selected confidence levels, the null hypothesis that this IMF is not distinguishable from the corresponding IMF of a white noise can be rejected. In other words, the decomposition result is statistically significant.

Here, each of the three records was decomposed into eight oscillatory components and a trend with EEMD (Figures 4-6). Then, another sifting was done on each IMF except the trend to confirm that the EEMD-produced results follow the conditions defining an IMF. Eventually, the statistical significance of each IMF (except IMF8 which is also a trend) was tested at 95% and 99% confidence levels (Figures 7-9). Empirically, the first IMF results from random noise; therefore, it is not considered in the discussion. However, it is still employed to compute the mean energy of the other IMFs.

For atmospheric $\Delta^{14}C$, IMF4 through IMF7 are above the 95% and 99% confidence level lines, and are considered statistically significant. IMF2 and IMF3 located on the 95% confidence level line are still physically meaningful. For total solar irradiance, IMF2 through IMF7 are above 95% and 99% confidence level lines and are all statistically significant. For DA $\delta^{18}O_{speleothem}$, IMF3 through IMF7 are above 95% and 99% confidence level lines and are statistically significant. IMF2 is located below the 95% confidence level line. Given the small deviation, it is still considered to be partially physically meaningful.

IMFs for total solar irradiance generally are more statistically significant than IMFs for atmospheric $\Delta^{14}C$. However, the estimation of which record best represents solar activity is beyond the scientific scope of this study. Therefore, the comparison between them is not discussed here. Because many similarities of the corresponding IMFs from both data can be identified with visual inspection, it is considered that both of them can represent solar activity during the Holocene.

IMF

To investigate the relationship between corresponding underlying processes for solar activity and Asian monsoon strength, the period of each IMF was quantified. Prior to obtaining the period of an IMF, the instantaneous frequency of each IMF was calculated with a Hilbert transform-produced analytic function (Huang and Wu, 2008) (Figures 10-12). The Hilbert transform of a function $x(t)$ of L^P class (pth powers of $x(t)$ must be integrable) is defined as:

$$y(t) = \frac{1}{\pi} P \int_{-\infty}^{\infty} \frac{x(\tau)}{t-\tau} d\tau$$

where P is the Cauchy principal value of the singular integral. Considering the Hilbert transform as the imaginary part, the analytic signal can be expressed as:

$$z(t) = x(t) + iy(t) = a(t)e^{i\theta(t)}$$

$$a(t) = (x^2 + y^2)^{1/2}$$

$$\theta(t) = \tan^{-1}\frac{y}{x}$$

where $i = \sqrt{-1}$, a and θ are instantaneous amplitude and phase. Instantaneous frequency then can be expressed as:

$$\omega = \frac{d\theta}{dt}$$

Subsequently, a probability density function for each instantaneous frequency was estimated with a normal kernel function. The instantaneous frequency of each IMF (except IMF1) is approximately normally distributed. The frequency distributions of corresponding IMFs have similar shapes (Figure 13). For a given IMF, the frequency with the highest density value was selected as its mean frequency. The mean period of each IMF was then obtained according to the mathematic relation between period and frequency (Tables 1 and 2). The period of IMF8 is so long that it is considered a trend within the 8,800-year period under investigation. The periods of the corresponding IMFs from the three proxy records (i.e., $\Delta^{14}C$, total solar irradiance, and DA $\delta^{18}O_{speleothem}$) are very similar. Given this, we hypothesize that the corresponding IMFs from the three records represent similar underlying processes within the data. Thus, WTC can be applied to each pair of the corresponding IMFs for coherence estimations. As a whole, the period of a given IMF is roughly half of that of the next IMF, which means EMD is a dyadic filter (Wu and Huang, 2004).

Coherence and phase relationship

The following data analysis is separated into two groups: (1) atmospheric $\Delta^{14}C$ and DA $\delta^{18}O_{speleothem}$; and (2) total solar irradiance (reconstructed from the ice core ^{10}Be record) and DA $\delta^{18}O_{speleothem}$. In the WTC plots, the high coherence between two signals is represented by the area bounded by the thick contour, which is the 0.05 significance level

against red noise. The local phase relationship is expressed by the arrows. Arrows pointing right represent in-phase, while arrows pointing left are anti-phase. If the first signal leads the second one by 90 degrees, arrows point straight up. In contrast, a 90-degree lag corresponds to the arrows pointing straight down. For a lead-lag relationship, only coherence areas with proper phase angle (45-90 degrees; i.e., the range between the diurnal/seasonal cycle and ice volume, respectively) are identified. Due to the edge artifacts, high coherence areas outside the COI or penetrating the COI are not meaningful. Hence, only high coherence areas with correct phase angles are presented in following sections.

$\Delta^{14}C$ and $\delta^{18}O_{speleothem}$ values

For IMF2, high coherence appears at 22-48 yr around 900-1000 yr BP, at 24-60 yr around 2000-2350 yr BP, at 24-40 yr around 3500-3600 yr BP, at 20-32 yr around 3800 yr BP, at 256-374 yr around 5250-6100 yr BP, at 20-40 yr around 5400-5500 yr BP, at 40-64 yr around 6500 yr BP, and at 50-128 yr around 7950-8500 yr BP (Figure 14). For IMF3, high coherence occurs at 32-60 yr around 6400 yr BP, at 256-384 yr around 7200-8200 yr BP, at 48-100 yr around 8000 yr BP, and at 40-56 yr around 8400 yr BP (Figure 15). For IMF4, high coherence is shown at 200-320 yr around 7200-8000 yr BP (Figure 16). For IMF5, high coherence is present at 64-96 yr around 750 yr BP and at 224-384 yr around 5100-5600 yr BP (Figure 17). For IMF6, there is high coherence at 100-192 yr around 4300-4750 yr BP and at 64-90 yr around 8000-8200 yr BP (Figure 18). IMF7 has no coherence (Figure 19). In sum, in time-frequency-IMF representation, the coherence between atmospheric $\Delta^{14}C$ and DA $\delta^{18}O_{speleothem}$ is low.

Total solar irradiance and $\delta^{18}O_{speleothem}$ values

For IMF2, high coherence is indicated at 24-56 yr around 7500-7600 yr BP (Figure 20). For IMF3, high coherence appears at 48-64 yr around 4750-4900 yr BP and at 48-80 yr around 5800-6000 yr BP (Figure 21). For IMF4, high coherence appears at 128-200 yr around 1250-1500 yr BP (Figure 22). For IMF5, high coherence occurs at 300-448 yr around 3500-4000 yr BP (Figure 23). For IMF6, no significant coherence is detected (Figure 24). For IMF7, there is high coherence at 340-426 yr around 5500-5900 yr BP and at 96-128 yr around 7200-7500 yr BP (Figure 25). Thus, in time-frequency-IMF representation, the coherence between total solar irradiance and DA $\delta^{18}O_{speleothem}$ is low.

Discussion

Our results demonstrate a weak link between solar activity and the Asian monsoon strength over the last 8,800 years, which is exemplified by low coherence in time-frequency-IMF representation. Previously reported causal links also rely on the frequency spectrum (Fleitmann et al., 2003; Wang et al., 2005; Cai et al., 2010). Wang et al. (2005) reported correlation at specific frequencies between detrended atmospheric $\Delta^{14}C$ and DA $\delta^{18}O_{speleothem}$ values with bivariate spectral analysis (see supporting online material for Wang et al. (2005)). The phase spectrum between detrended atmospheric $\Delta^{14}C$ and DA $\delta^{18}O_{speleothem}$ values was not discussed. As a complement, the cross-coherence and phase spectrum between atmospheric $\Delta^{14}C$ and DA $\delta^{18}O_{speleothem}$ raw data are also measured in the present study. For congruity, the SPECTRUM program using same parameters was applied (Schulz and

Stattegger, 1997; Wang et al., 2005). The correspondence between atmospheric $\Delta^{14}C$ and DA $\delta^{18}O_{speleothem}$ at each frequency is expressed with the squared coherency, which is estimated with Lomb-Scargle Fourier transform for unevenly spaced time series, associated with a Welch-Overlapped-Segment-Averaging procedure. The value of the squared coherency ranges between 0 and 1, in which 0 means no correlation and 1 presents highest correlation at the corresponding frequencies. Overall, the coherence between atmospheric $\Delta^{14}C$ and DA $\delta^{18}O_{speleothem}$ is not high. High coherence with 95% false alarm level only occurs at 57 and 20 yr in which the squared coherency equals 0.45 and 0.54 respectively (Figure 26). For the phase spectrum (figure is not shown), $\Delta^{14}C$ leads DA $\delta^{18}O_{speleothem}$ values by -109 degrees at 57 yr and 28 degrees at 20 yr. In sum, the spectral coherency between atmospheric $\Delta^{14}C$ and DA $\delta^{18}O_{speleothem}$ is low, and the phase angles are not meaningful.

Conclusions

Insignificant covariance between atmospheric $\Delta^{14}C$ and DA $\delta^{18}O_{speleothem}$ record at the 95% confidence level shows no linear and stationary relationship between solar activity and Asian monsoon strength during the Holocene (Haam and Huybers, 2010). However, any relationships between nonlinear and nonstationary processes hidden within the data were not estimated in Haam and Huybers (2010). Using an a posteriori and adaptive basis, EEMD decomposes the nonlinear and nonstationary records for solar activity and Asian monsoon strength into a series of physically meaningful underlying processes, and the coherence and phase between corresponding processes are inspected quantitatively with WTC. The results indicate nonlinear and nonstationary relationship between solar activity and Asian monsoon

strength over the last 8,800 years is insignificant. Our study supports that a causal relationship does not exist between solar activity and Asian monsoon strength during the Holocene.

Acknowledgements

We appreciate comments for data analysis from Norden Huang, John Moore, Richard Smith, and Zhaohua Wu. This work was supported by the Martin Research Fellowship from the Department of Geological Sciences, University of North Carolina at Chapel Hill.

Table 1. Periods for IMFs of atmospheric $\Delta^{14}C$ and DA $\delta^{18}O_{speleothem}$ record

$\Delta^{14}C$		$\delta^{18}O$	
Components	Period (year)	Components	Period (year)
IMF2	73 ± 344	IMF2	72 ± 430
IMF3	124 ± 553	IMF3	141 ± 566
IMF4	258 ± 674	IMF4	238 ± 943
IMF5	658 ± 1812	IMF5	575 ± 3017
IMF6	864 ± 2591	IMF6	1206 ± 3810
IMF7	2380 ± 4454	IMF7	2508 ± 14388
IMF8	7393 ± 30769	IMF8	12211 ± 31746

Table 2. Periods for IMFs of total solar irradiance and DA $\delta^{18}O_{speleothem}$ record

Total solar irradiance		$\delta^{18}O$	
Components	Period (year)	Components	Period (year)
IMF2	79 ± 284	IMF2	72 ± 430
IMF3	144 ± 522	IMF3	141 ± 566
IMF4	286 ± 1411	IMF4	238 ± 943
IMF5	818 ± 1757	IMF5	575 ± 3017
IMF6	1448 ± 6849	IMF6	1206 ± 3810
IMF7	2236 ± 11364	IMF7	2508 ± 14388
IMF8	11241 ± 68966	IMF8	12211 ± 31746

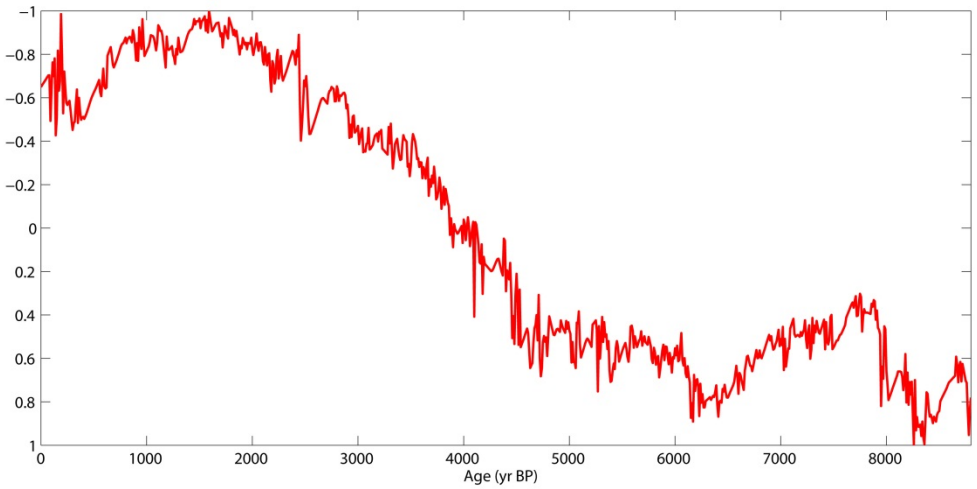

Figure 1. Atmospheric $\Delta^{14}C$ over the last 8,800 years (Stuiver et al., 1998)

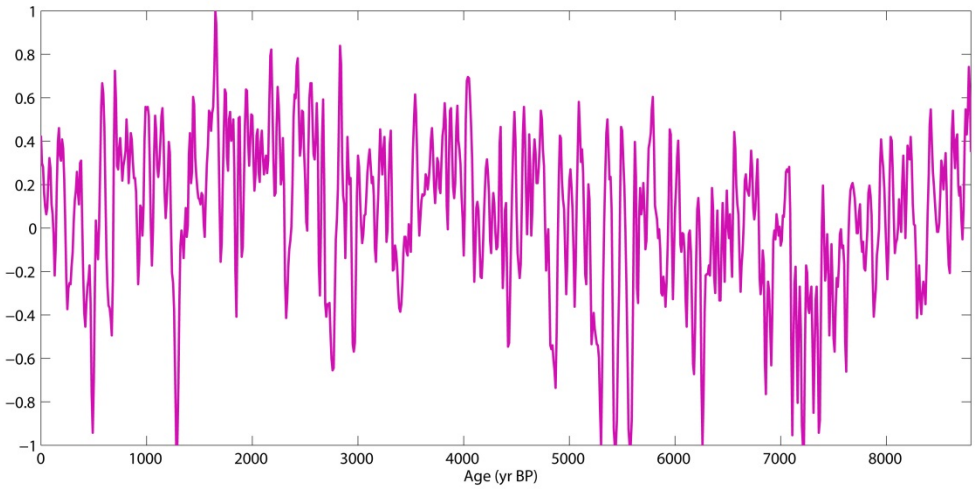

Figure 2. Total solar irradiance over the last 8,800 years (Steinhilber et al., 2009)

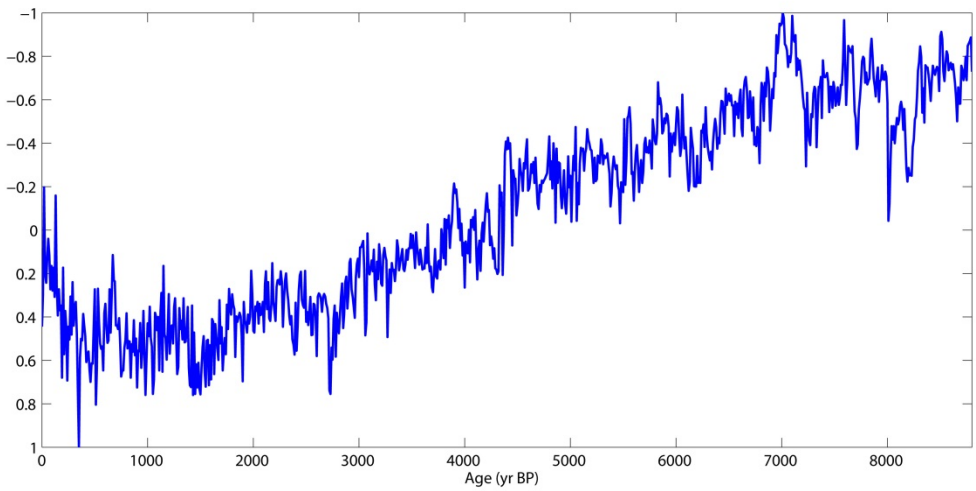

Figure 3. Stalagmite DA $\delta^{18}O$ from Dongge Cave, China, over the last 8,800 years (Wang et al., 2005)

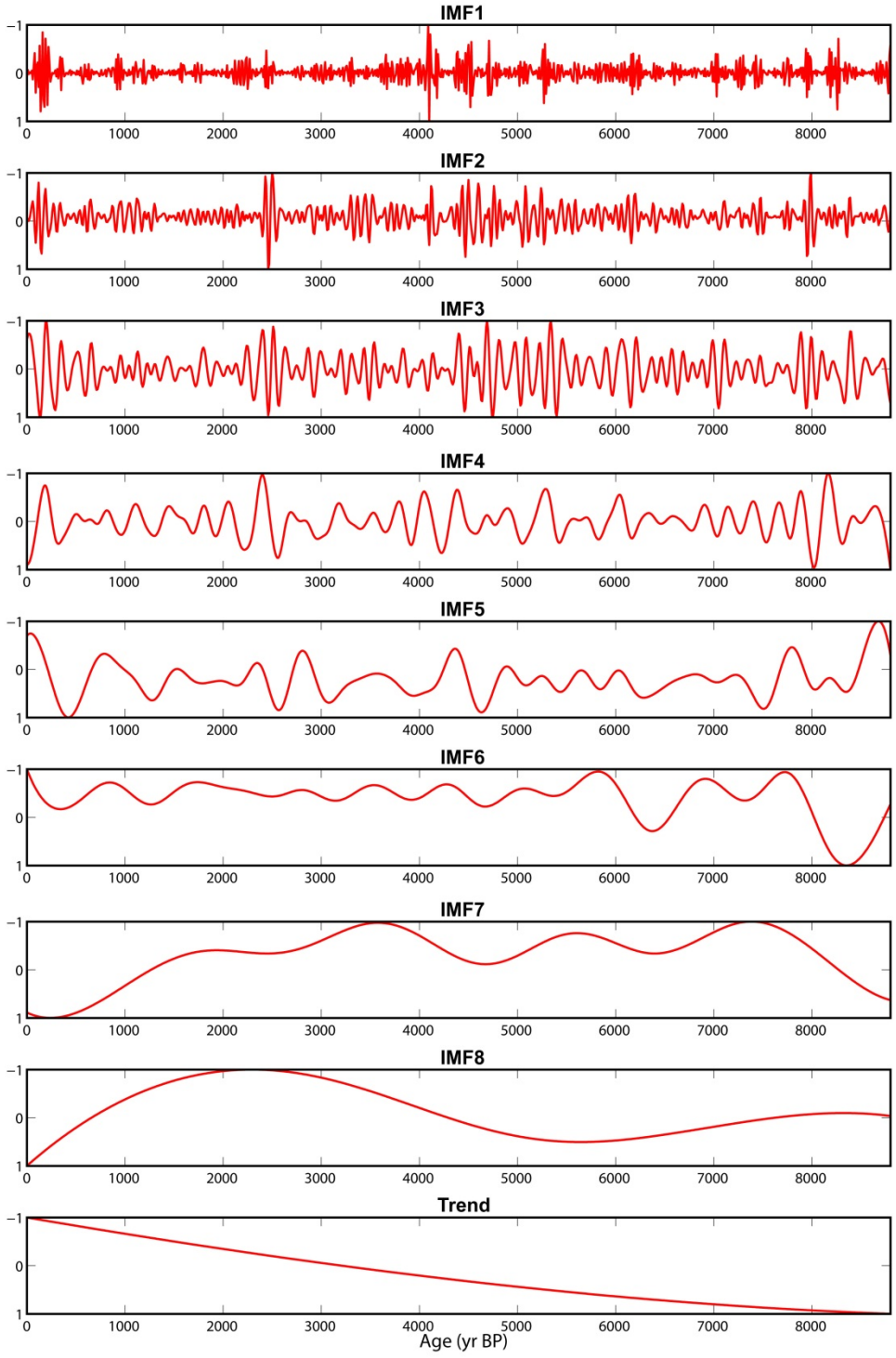

Figure 4. IMFs and the trend of atmospheric $\Delta^{14}C$. In EEMD, the ratio of white noise's stand deviation to that of the data is 0.5 and the ensemble number is 1000.

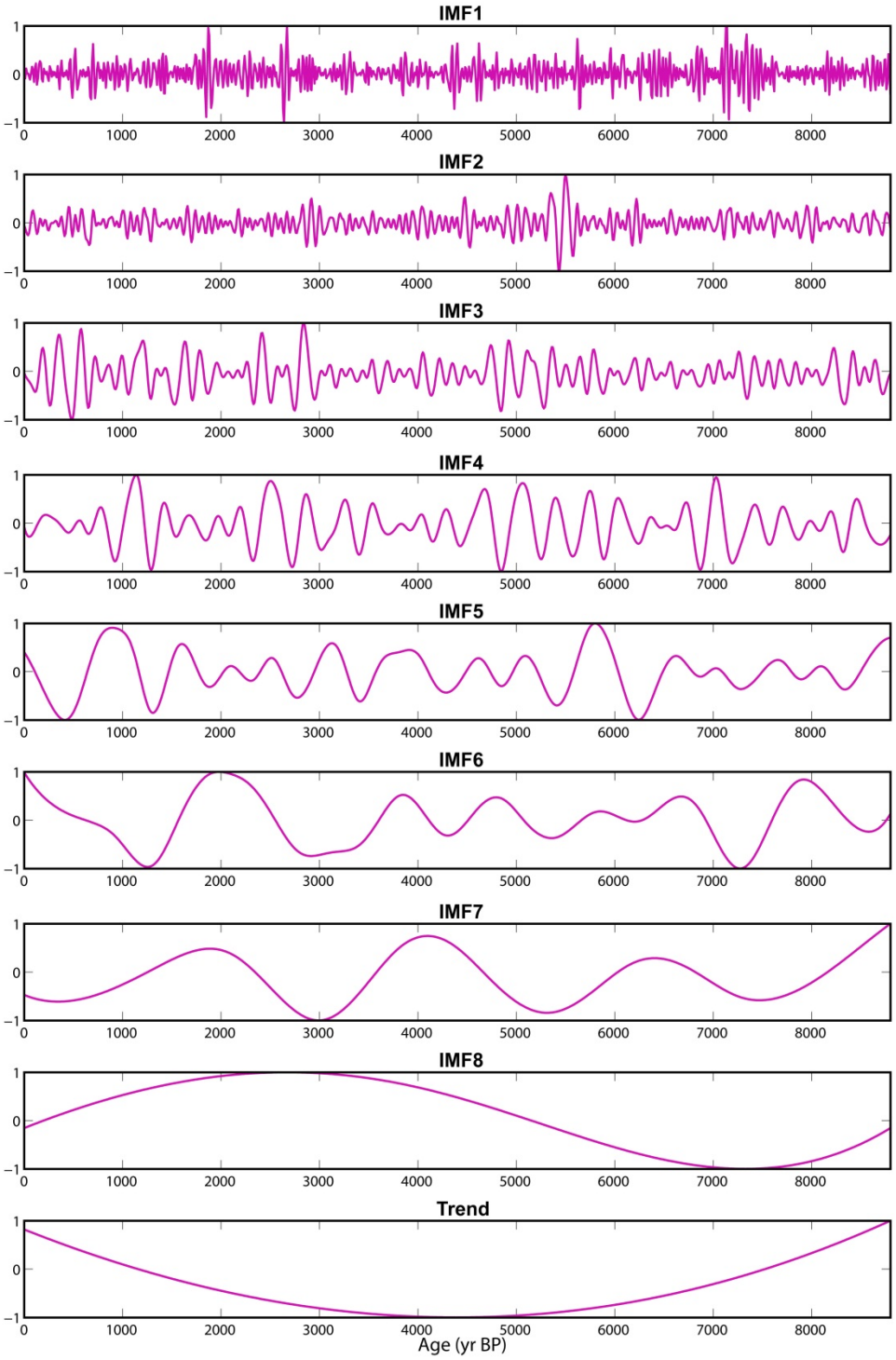

Figure 5. IMFs and the trend of total solar irradiance

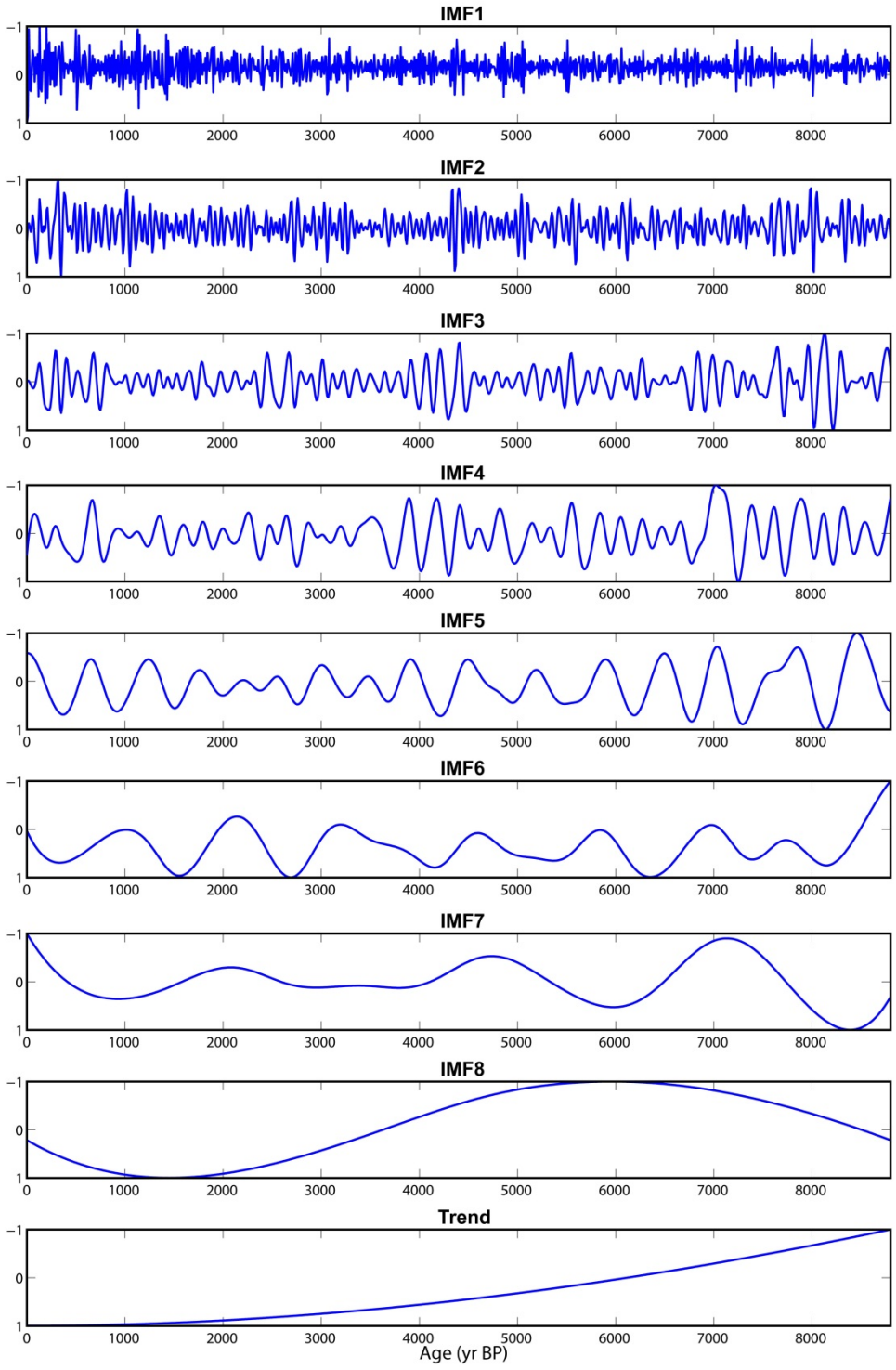

Figure 6. IMFs and the trend of DA $\delta^{18}O_{speleothem}$

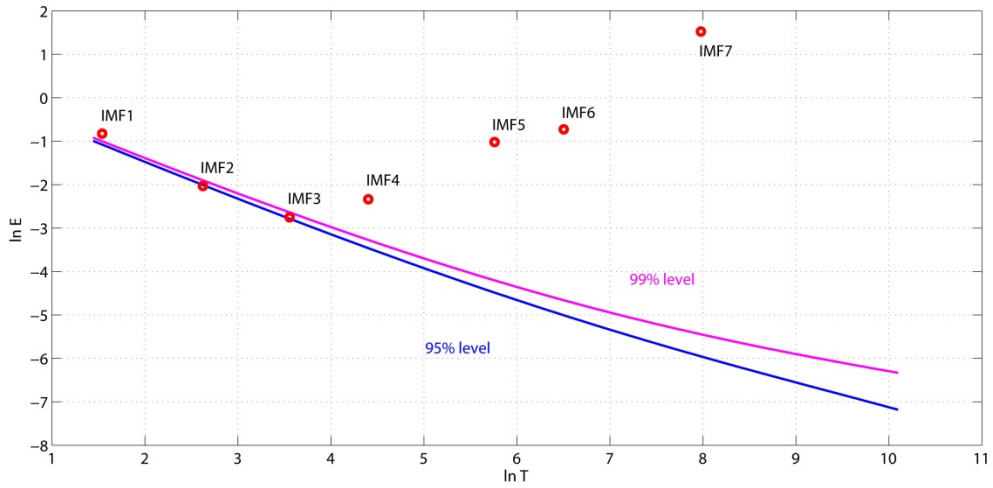

Figure 7. Significance test of IMFs of atmospheric $\Delta^{14}C$. Since IMF1 is a random noise, it is not considered in the discussion. However, here it is employed to compute the mean energy of the other IMFs. IMF4 through IMF7 are above the 95% and 99% confidence level lines, and are considered statistically significant. IMF2 and IMF3 located on the 95% confidence level line are still physically meaningful.

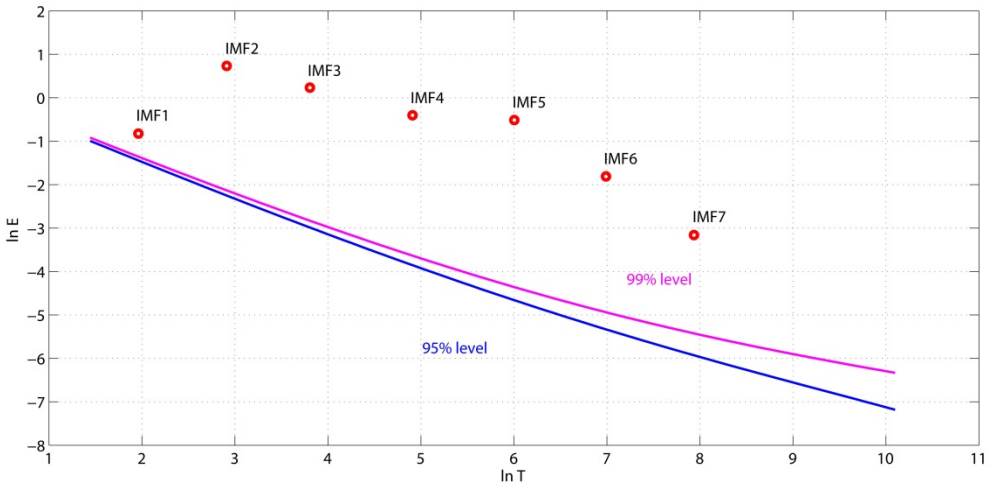

Figure 8. Significance test of IMFs of total solar irradiance. IMF2 through IMF7 are above 95% and 99% confidence level lines and are all statistically significant.

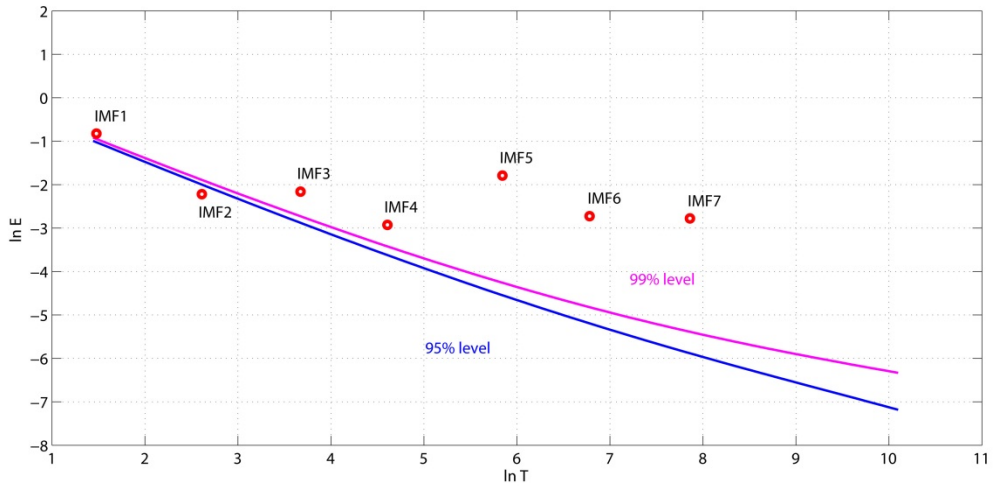

Figure 9. Significance test of IMFs of DA $\delta^{18}O_{speleothem}$. IMF3 through IMF7 are above 95% and 99% confidence level lines and are statistically significant. IMF2 is located below the 95% confidence level line. Given the small deviation, it is still considered to be partially physically meaningful.

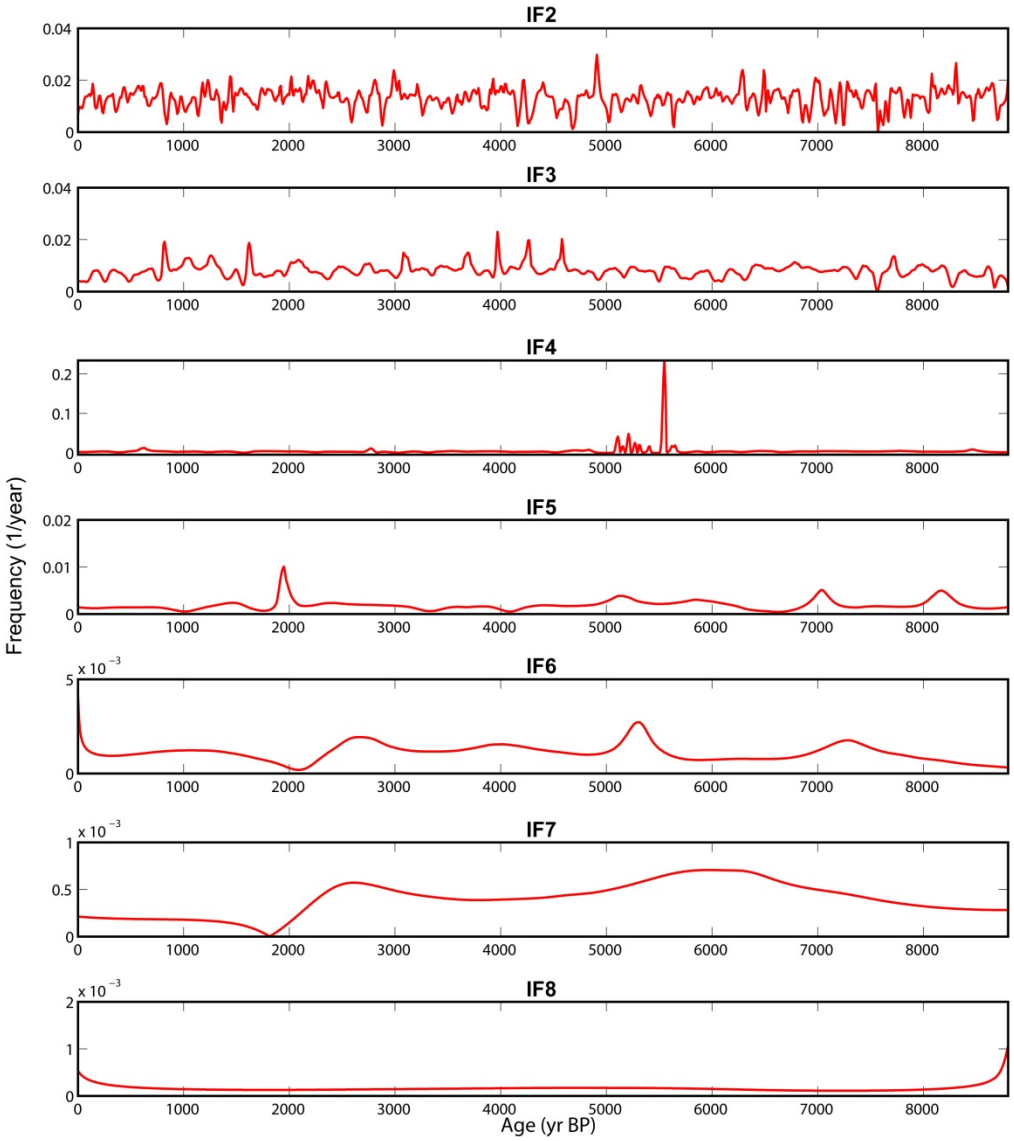

Figure 10. Instantaneous frequency of atmospheric $\Delta^{14}C$ IMF2-8

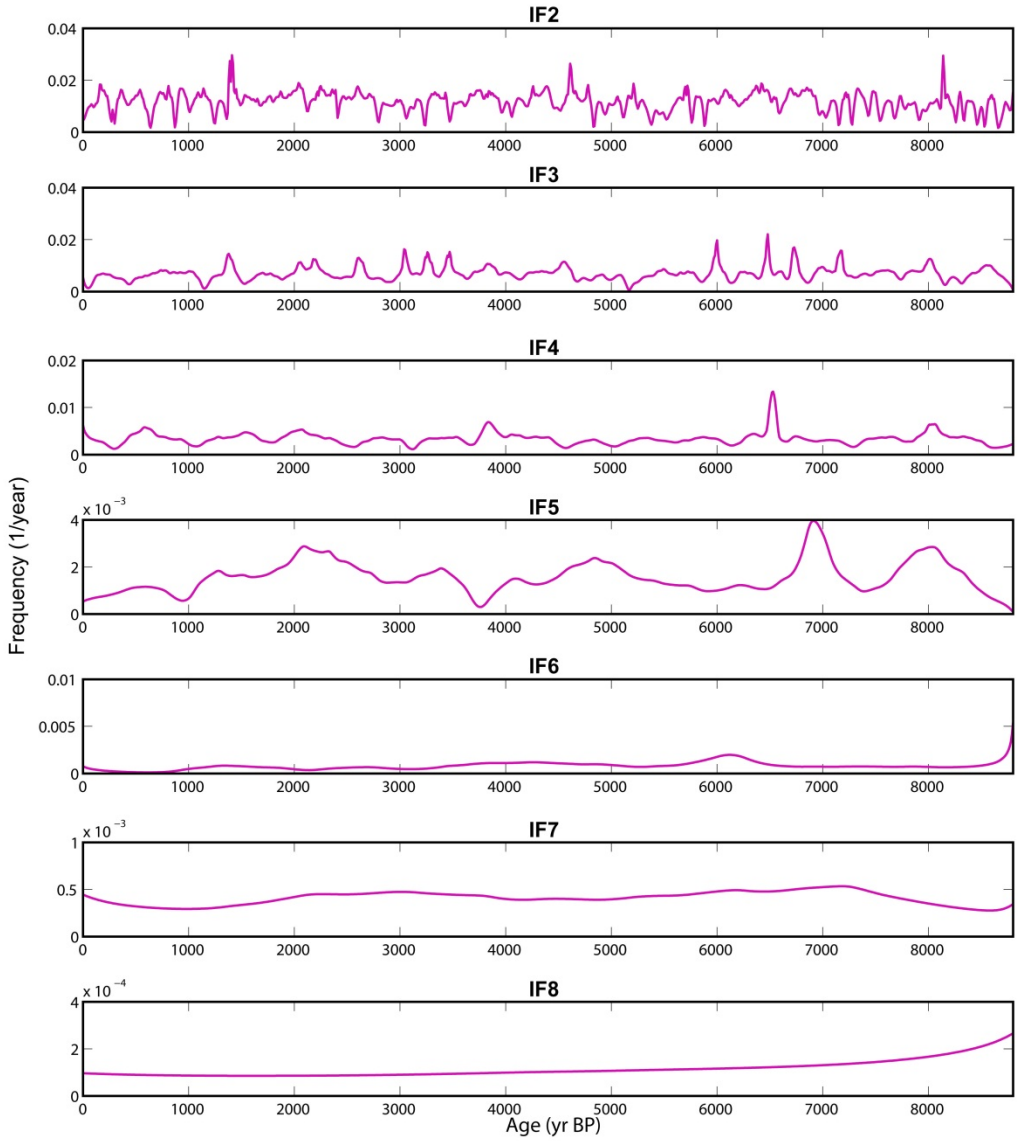

Figure 11. Instantaneous frequency of total solar irradiance IMF2-8

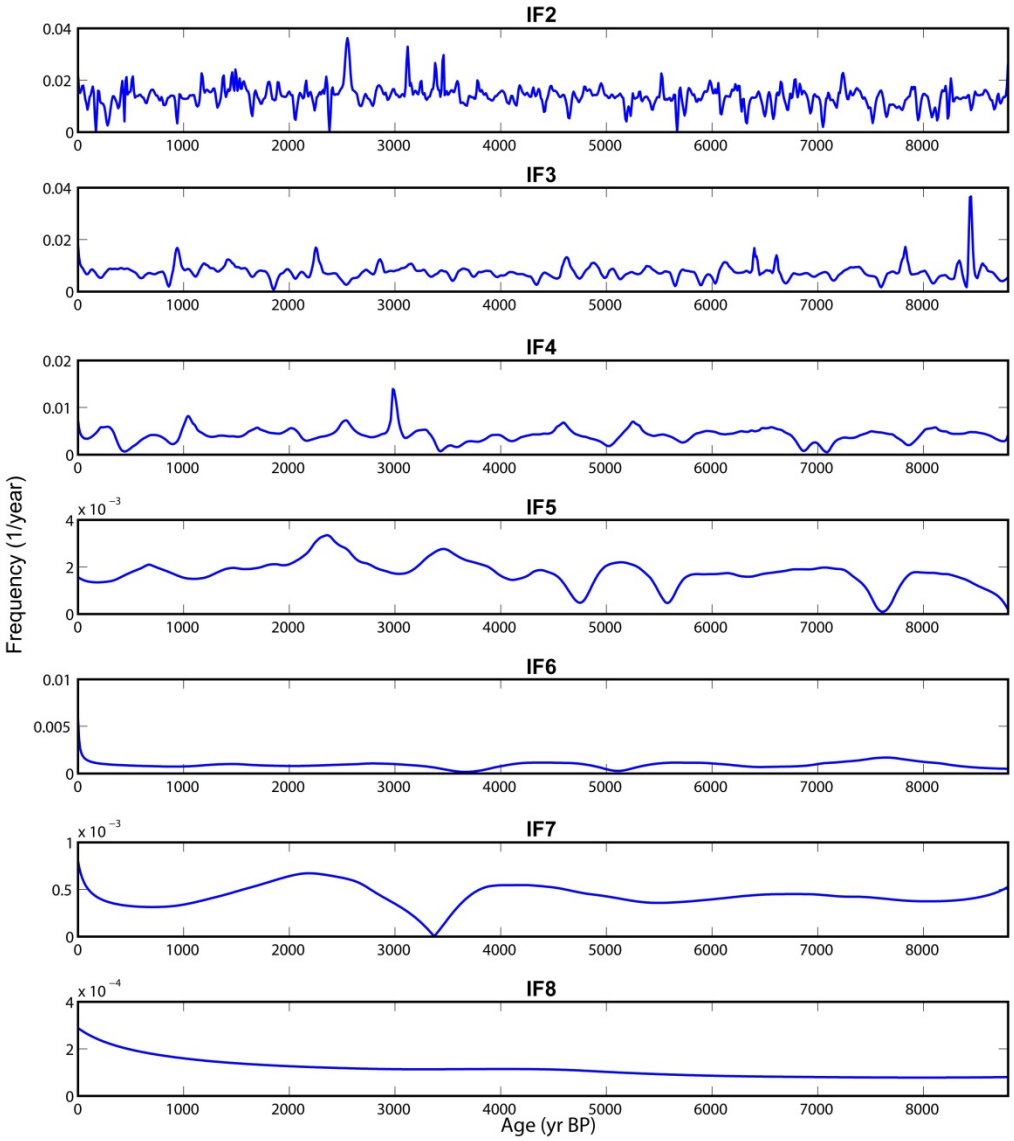

Figure 12. Instantaneous frequency of DA $\delta^{18}O_{speleothem}$ IMF2-8

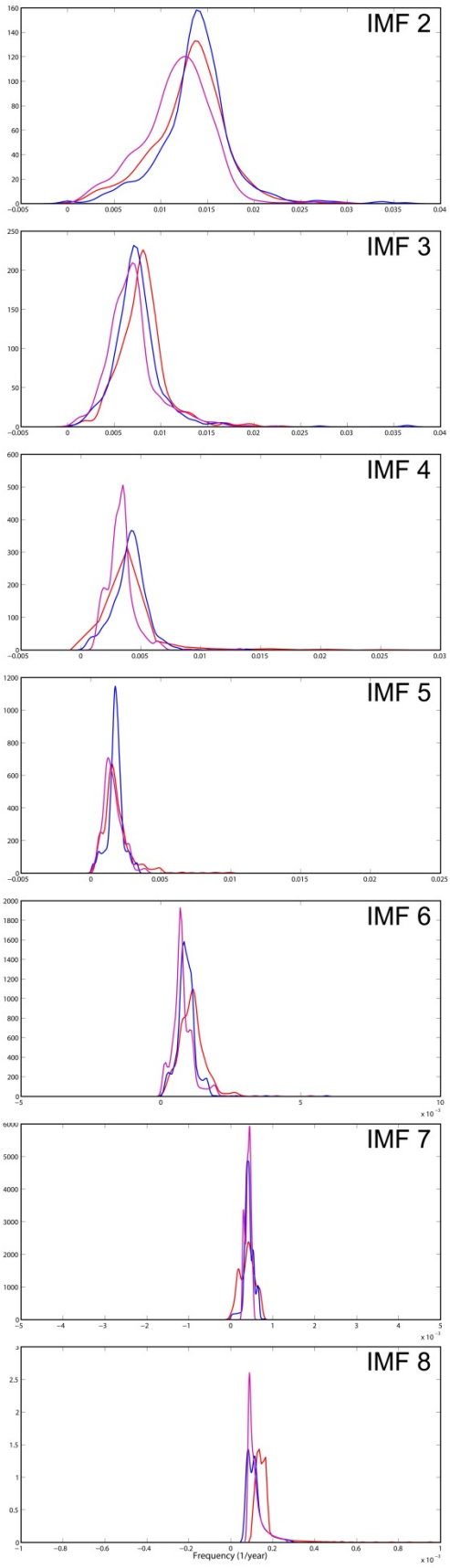
IMF 2
IMF 3
IMF 4
IMF 5
IMF 6
IMF 7
IMF 8
Frequency (1/year)

Figure 13. Comparison for frequency distribution of corresponding IMF2-8 (red: $\Delta^{14}C$, fuschia: total solar irradiance, blue: $\delta^{18}O_{speleothem}$)

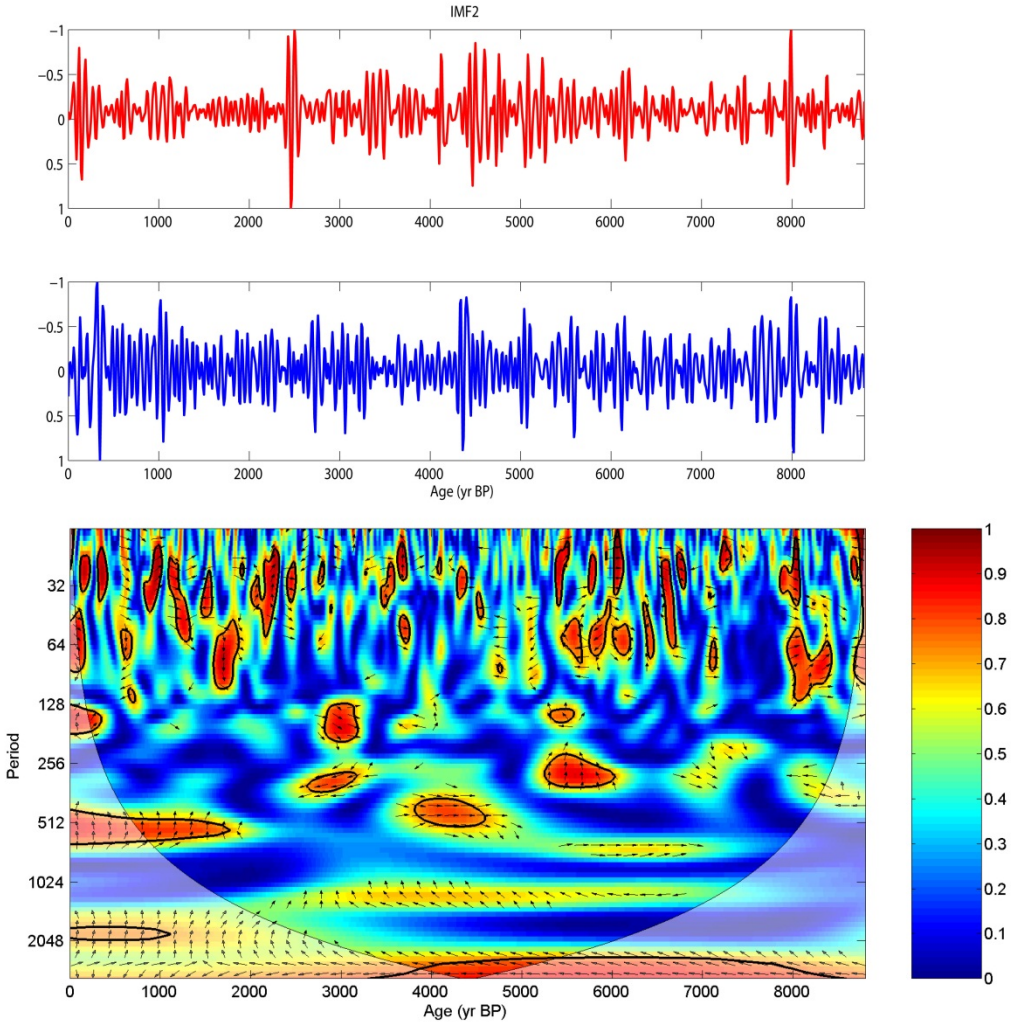

Figure 14. WTC for IMF2 of atmospheric $\Delta^{14}C$ and DA $\delta^{18}O_{speleothem}$. The area with the thick contour indicates high coherence. The contour means the 0.05 significance level against red noise. The local phase relationship is expressed by the arrows. Arrows pointing right are in-phase, while arrows pointing left are anti-phase. The first signal leading the second one by 90 degrees results in arrows pointing straight up, while a 90-degree lag corresponds to the arrows pointing straight down. High coherence appears at 22-48 yr around 900-1000 yr BP, at 24-60 yr around 2000-2350 yr BP, at 24-40 yr around 3500-3600 yr BP, at 20-32 yr around 3800 yr BP, at 256-374 yr around 5250-6100 yr BP, at 20-40 yr around 5400-5500 yr BP, at 40-64 yr around 6500 yr BP, and at 50-128 yr around 7950-8500 yr BP.

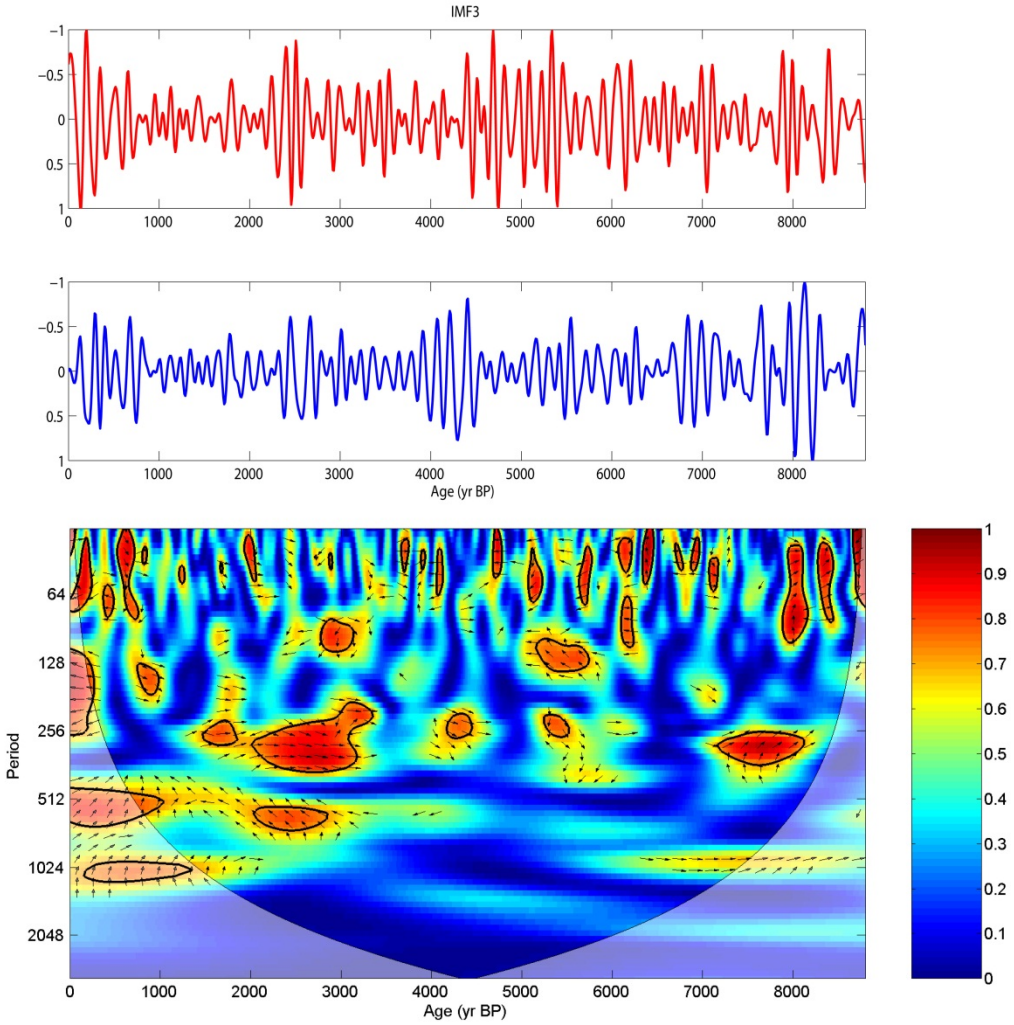

Figure 15. WTC for IMF3 of atmospheric $\Delta^{14}C$ and DA $\delta^{18}O_{speleothem}$. High coherence occurs at 32-60 yr around 6400 yr BP, at 256-384 yr around 7200-8200 yr BP, at 48-100 yr around 8000 yr BP, and at 40-56 yr around 8400 yr BP.

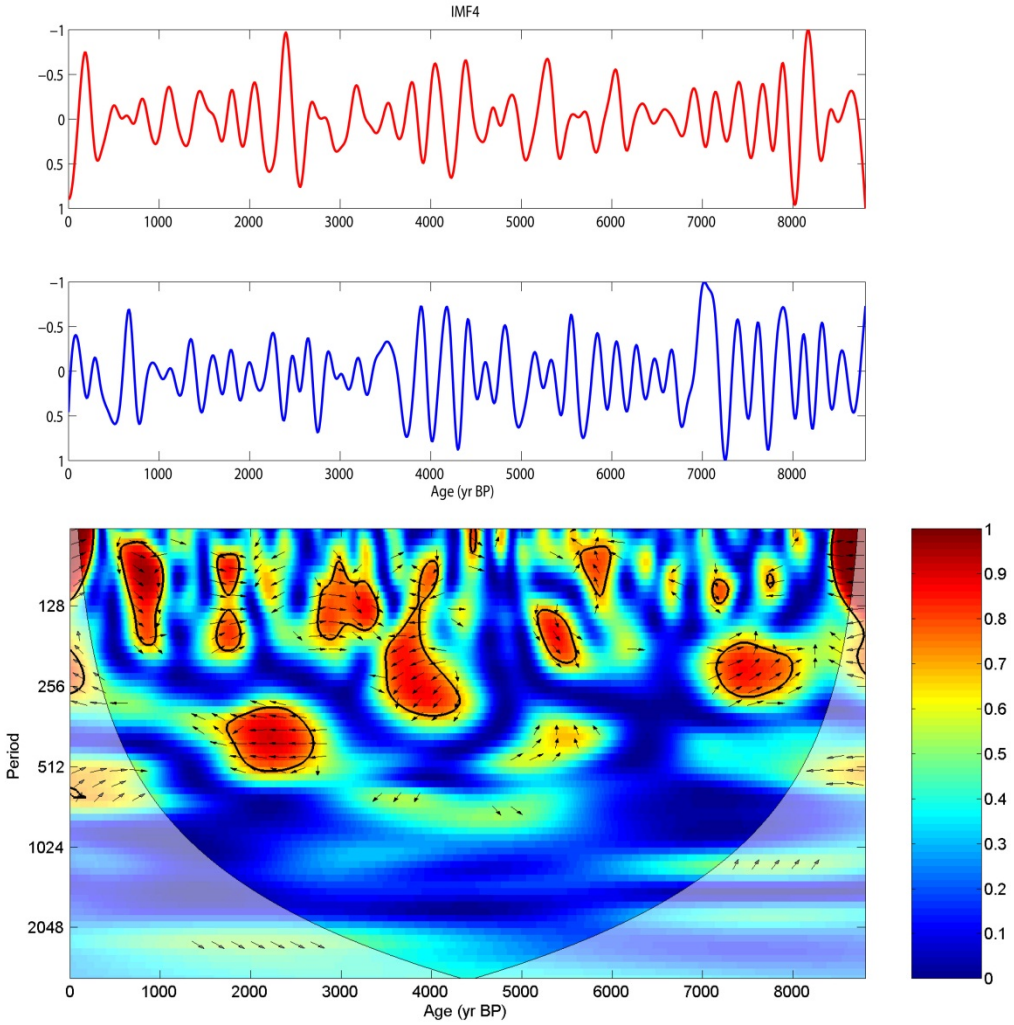

Figure 16. WTC for IMF4 of atmospheric $\Delta^{14}C$ and DA $\delta^{18}O_{speleothem}$. High coherence is shown at 200-320 yr around 7200-8000 yr BP.

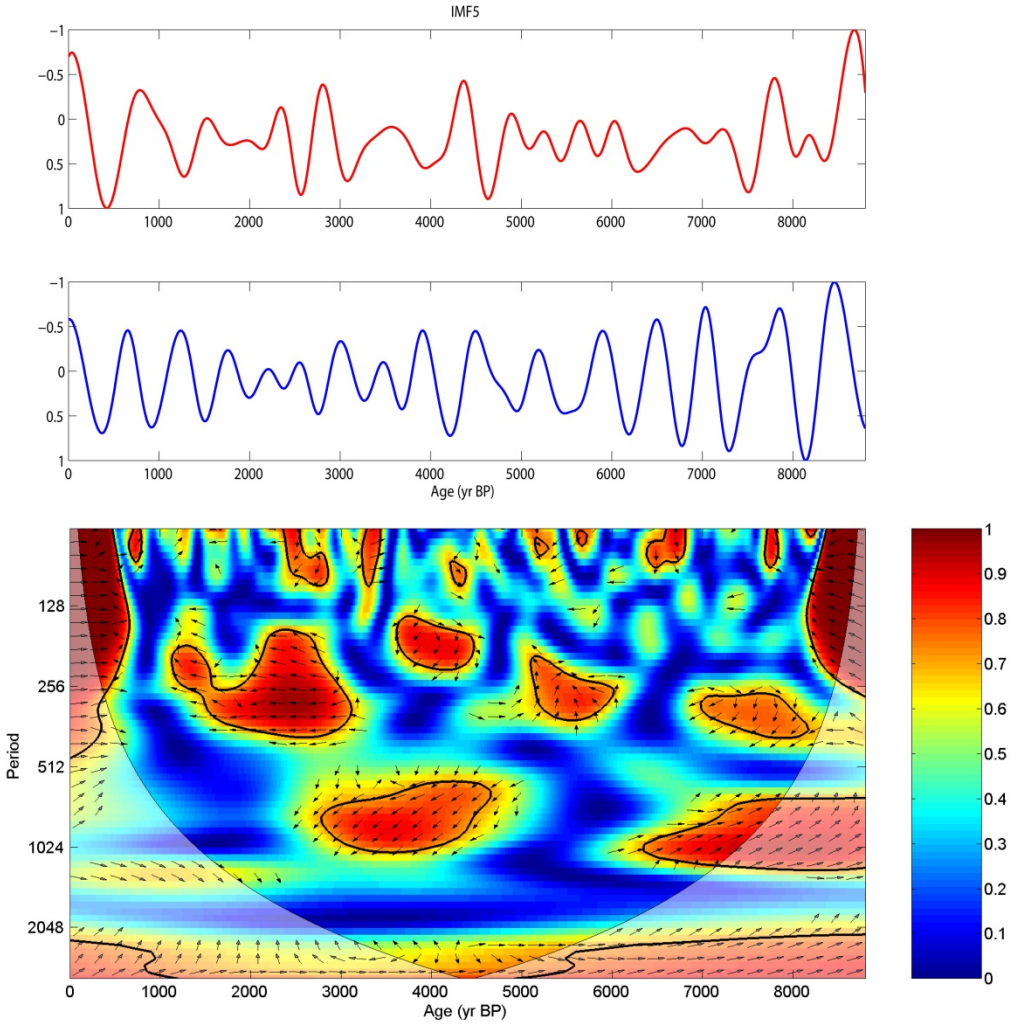

Figure 17. WTC for IMF5 of atmospheric $\Delta^{14}C$ and DA $\delta^{18}O_{speleothem}$. High coherence is present at 64-96 yr around 750 yr BP and at 224-384 yr around 5100-5600 yr BP.

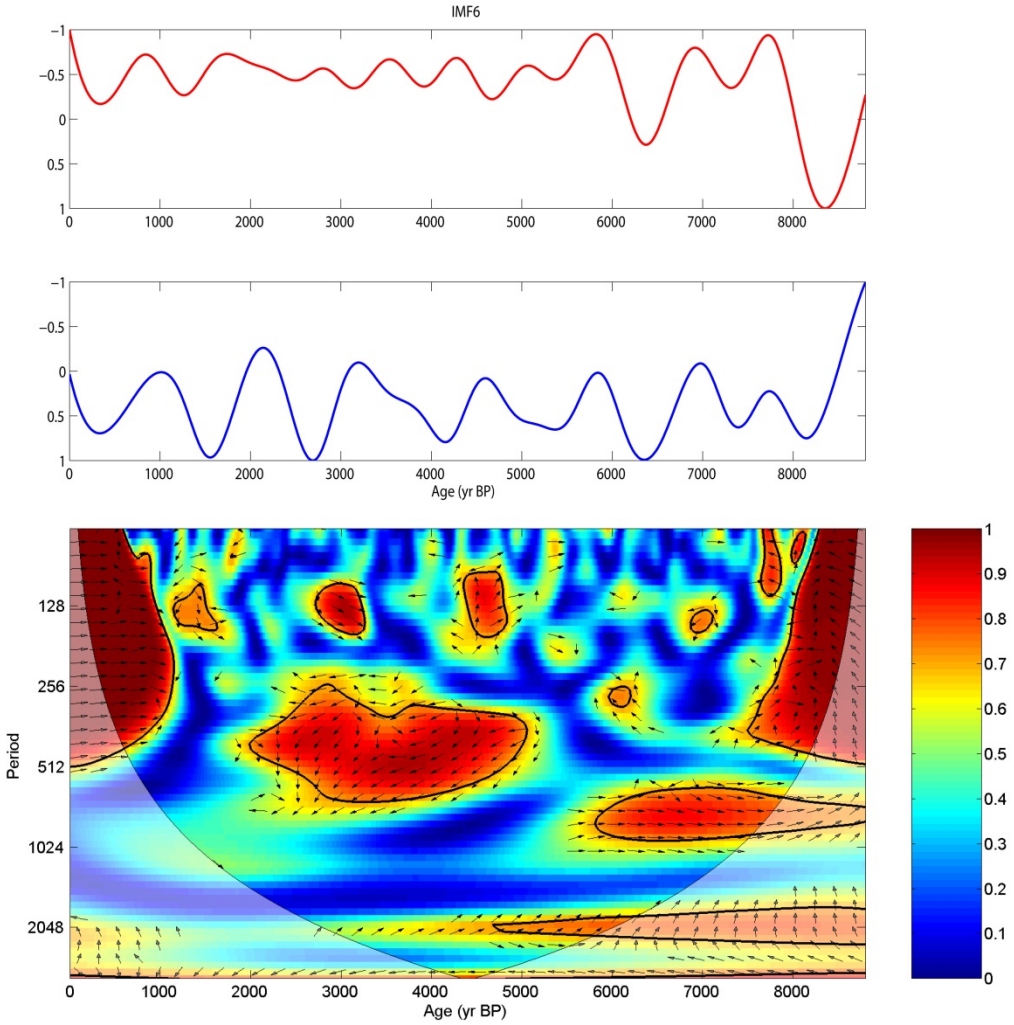

Figure 18. WTC for IMF6 of atmospheric $\Delta^{14}C$ and DA $\delta^{18}O_{speleothem}$. There is high coherence at 100-192 yr around 4300-4750 yr BP and at 64-90 yr around 8000-8200 yr BP.

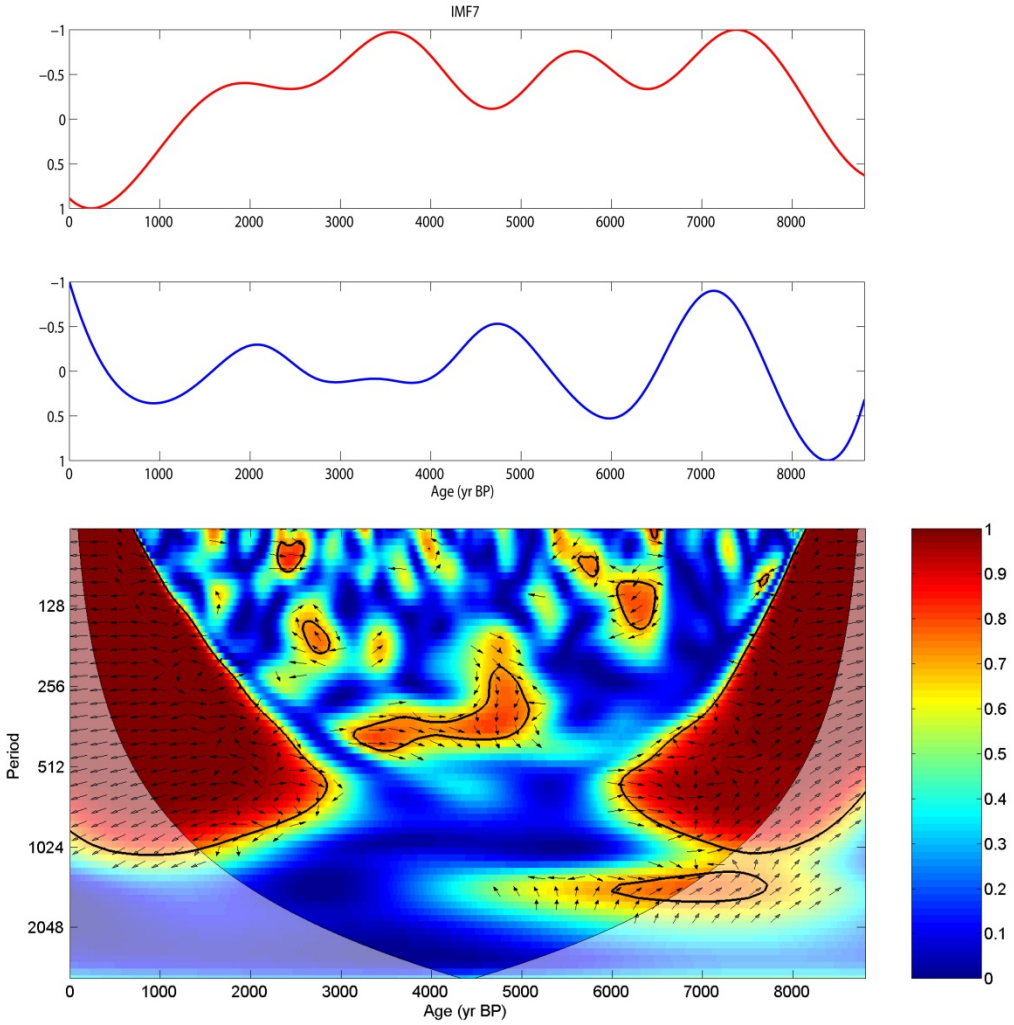

Figure 19. WTC for IMF7 of atmospheric $\Delta^{14}C$ and DA $\delta^{18}O_{speleothem}$. No coherence exists.

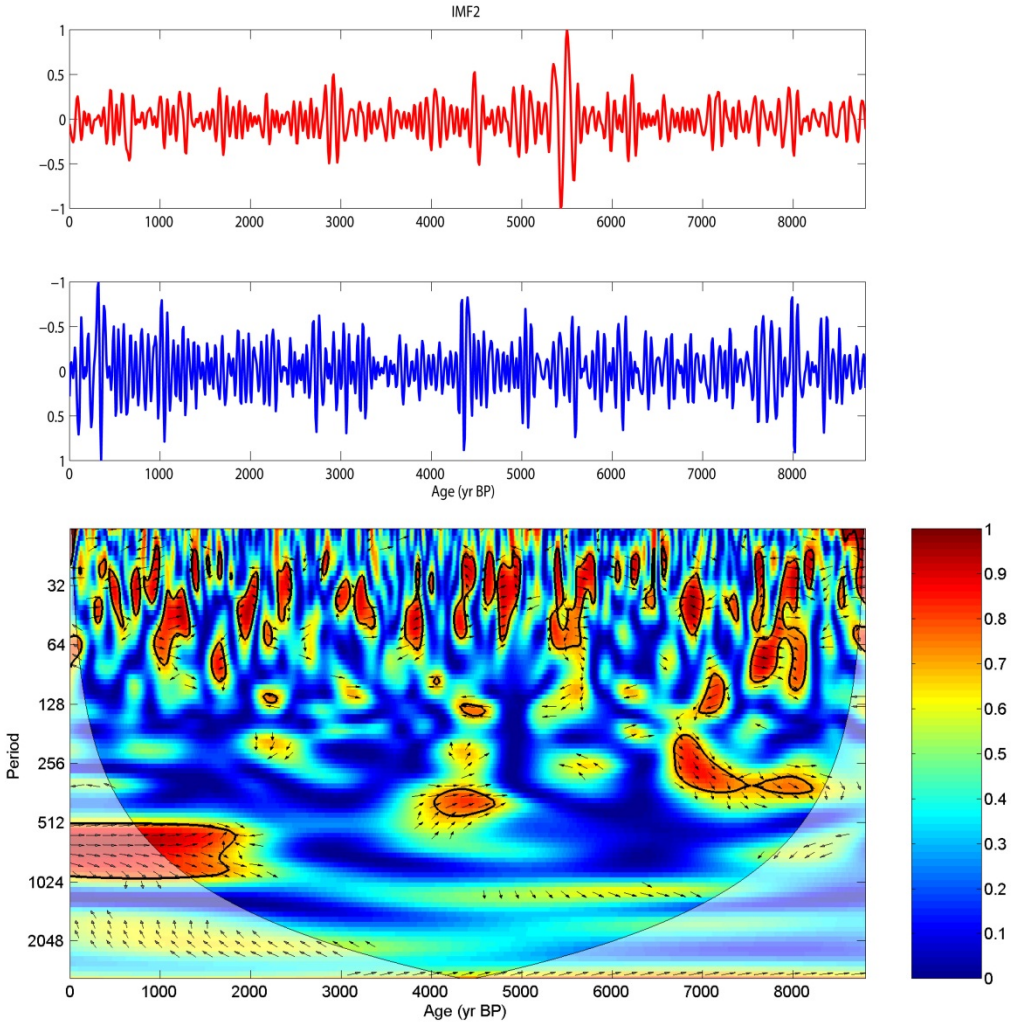

Figure 20. WTC for IMF2 of total solar irradiance and DA $\delta^{18}O_{speleothem}$. High coherence is indicated at 24-56 yr around 7500-7600 yr BP.

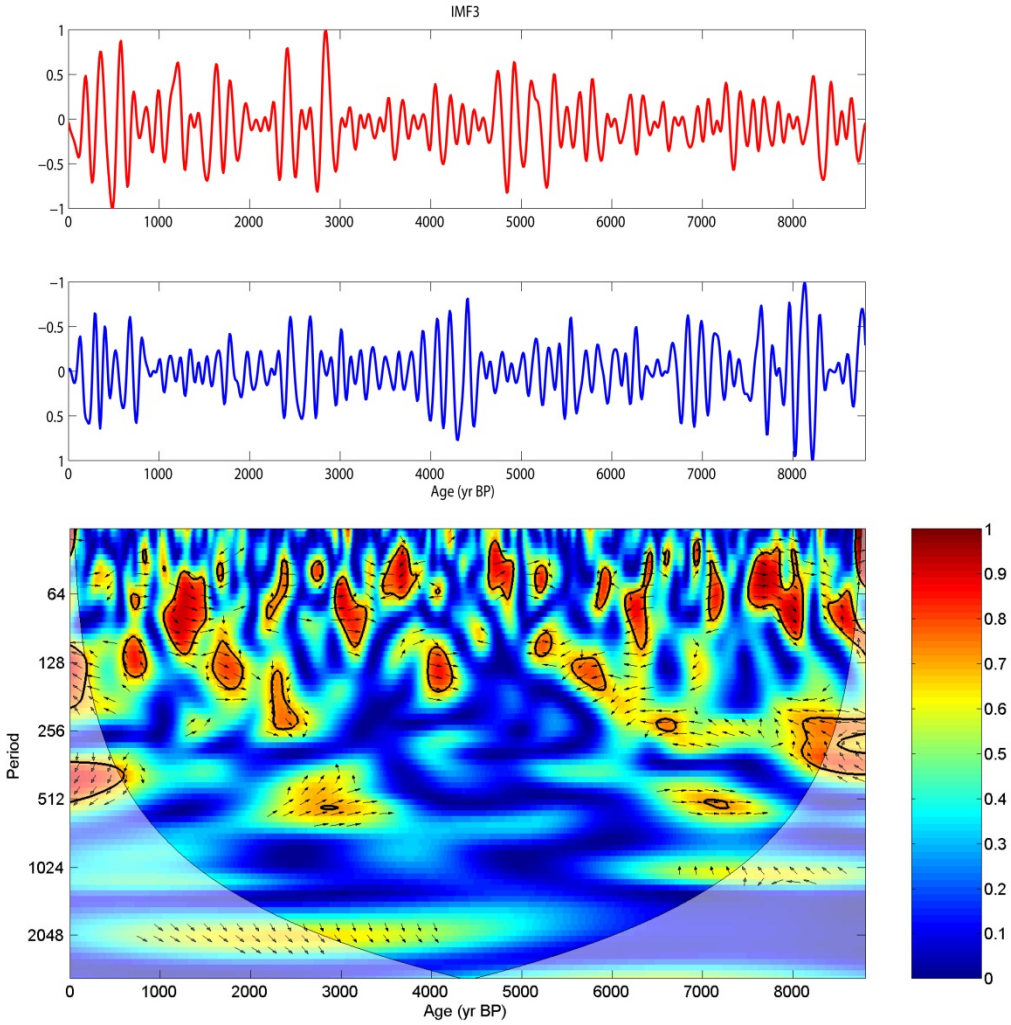

Figure 21. WTC for IMF3 of total solar irradiance and DA $\delta^{18}O_{speleothem}$. High coherence appears at 48-64 yr around 4750-4900 yr BP and at 48-80 yr around 5800-6000 yr BP.

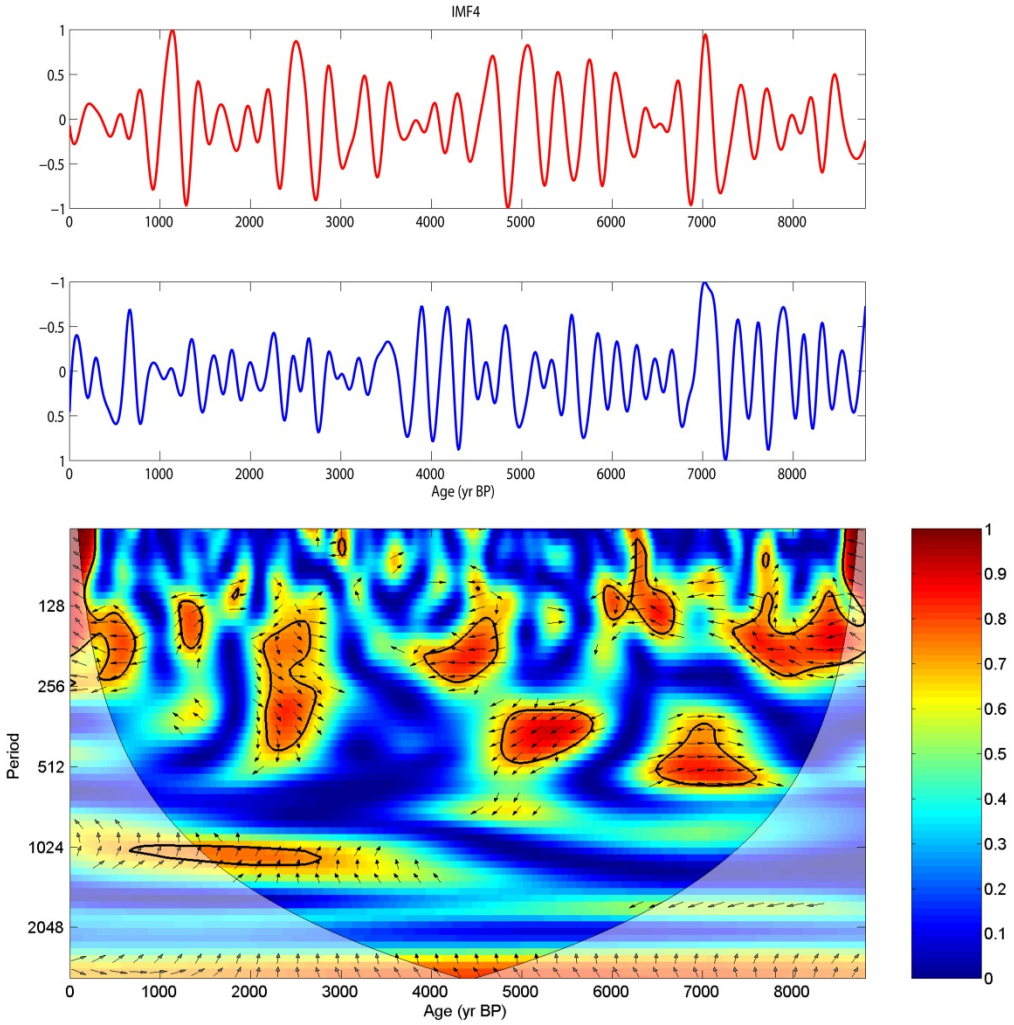

Figure 22. WTC for IMF4 of total solar irradiance and DA $\delta^{18}O_{speleothem}$. High coherence appears at 128-200 yr around 1250-1500 yr BP.

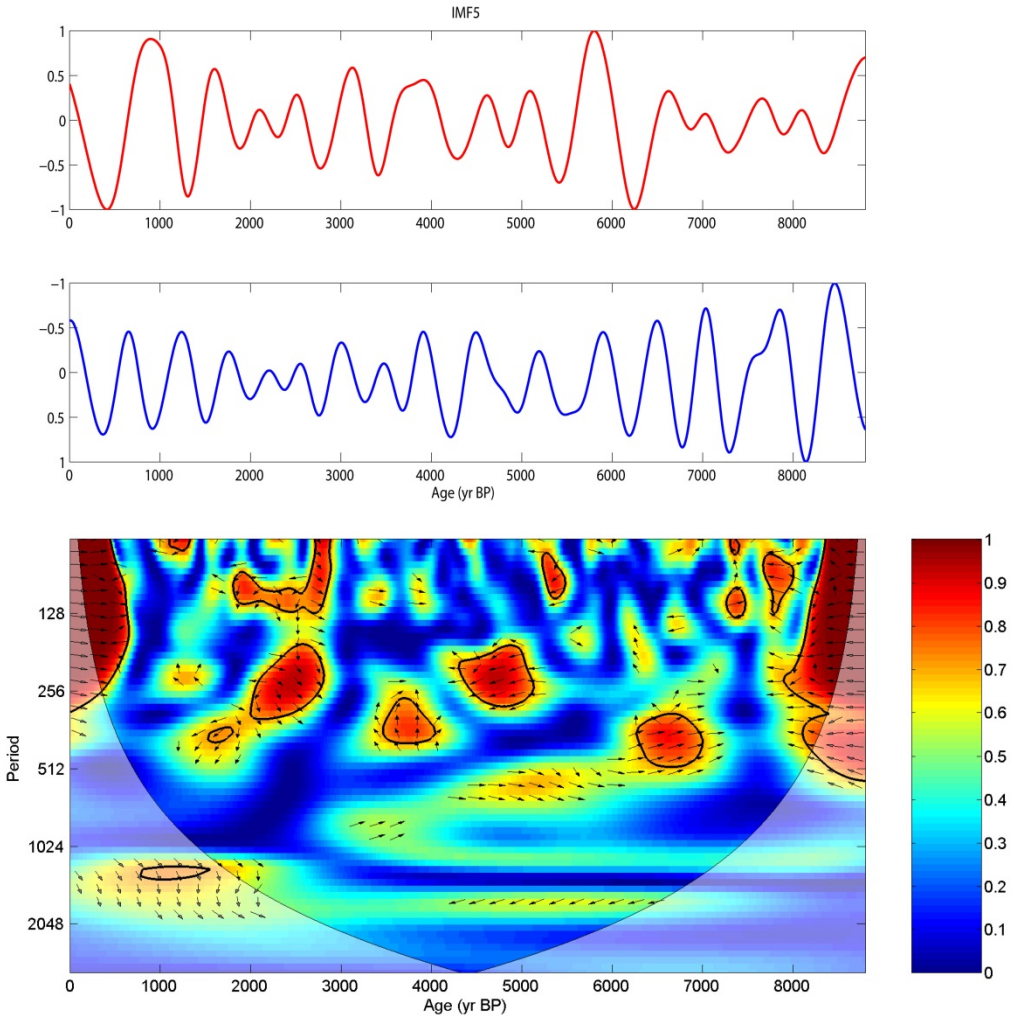

Figure 23. WTC for IMF5 of total solar irradiance and DA $\delta^{18}O_{speleothem}$. High coherence occurs at 300-448 yr around 3500-4000 yr BP.

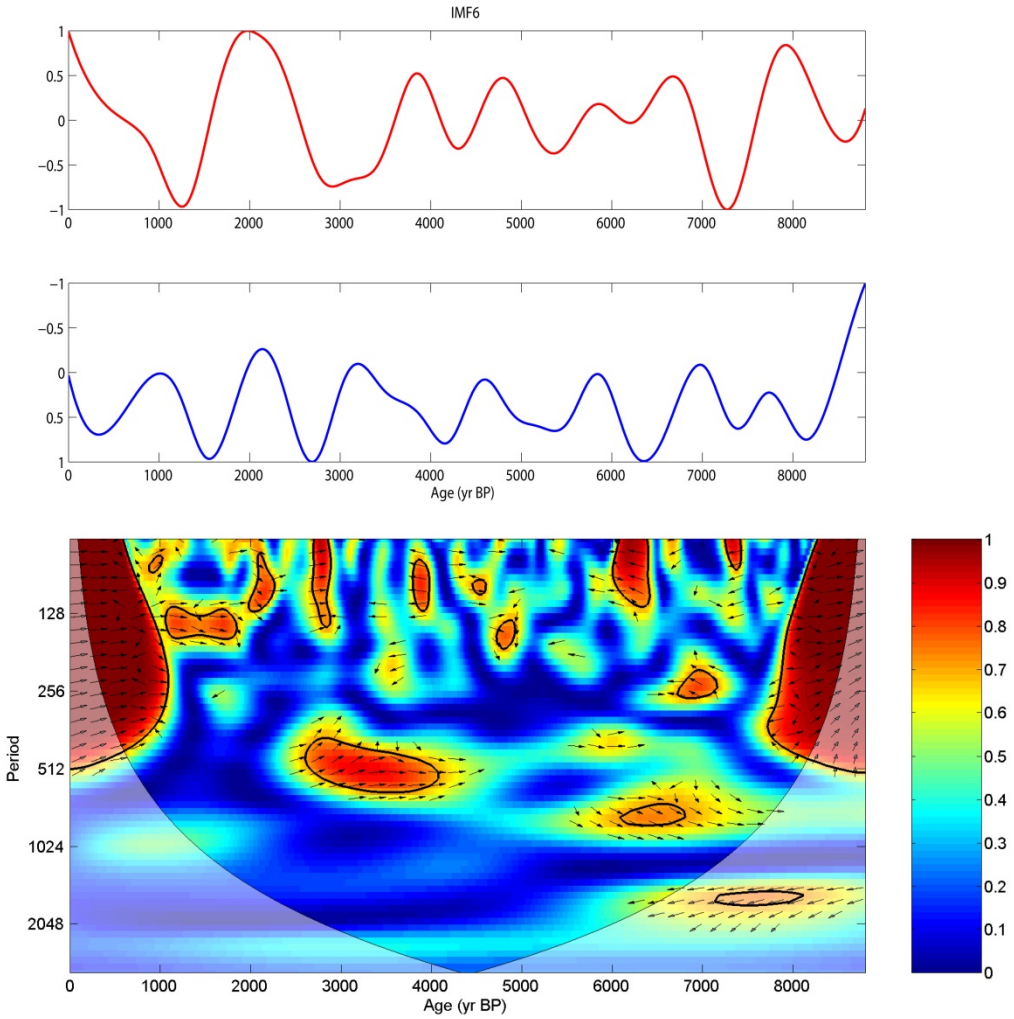

Figure 24. WTC for IMF6 of total solar irradiance and DA $\delta^{18}O_{speleothem}$. No significant coherence is detected.

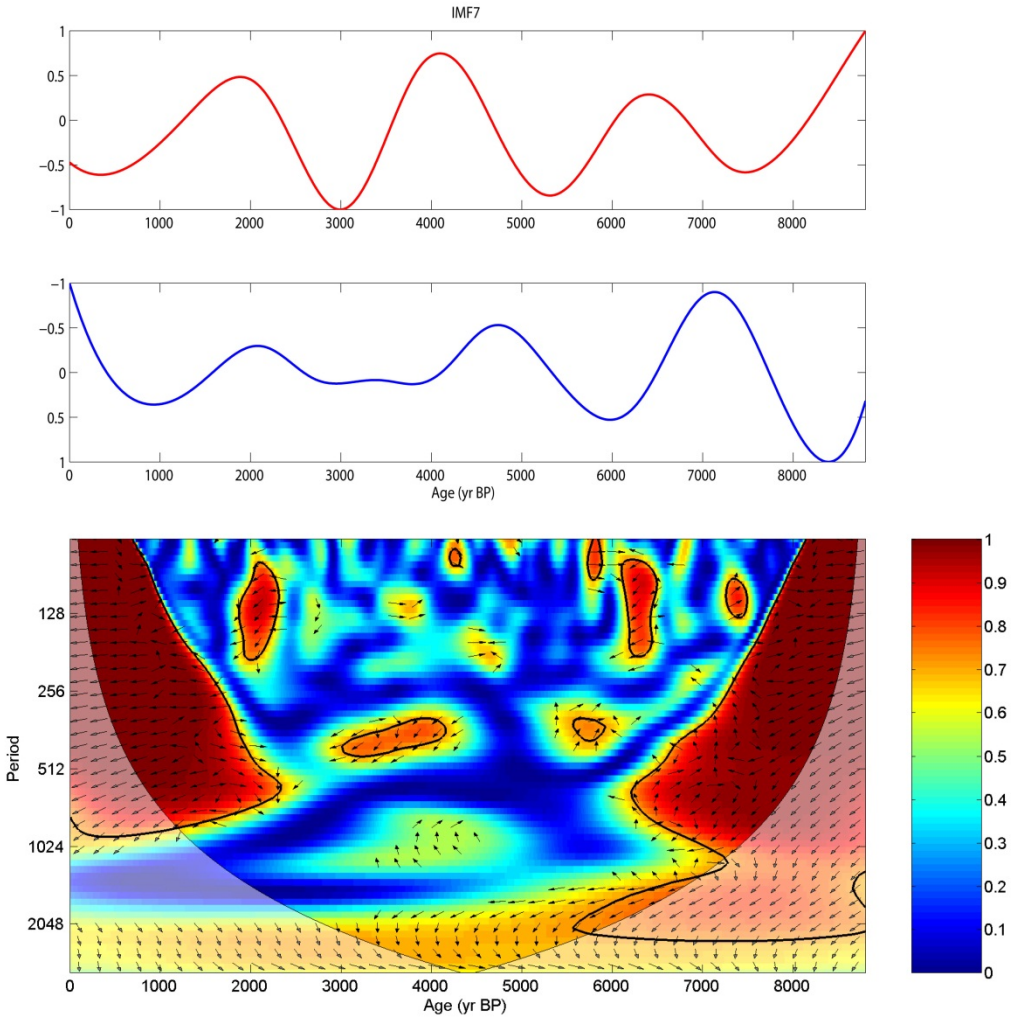

Figure 25. WTC for IMF7 of total solar irradiance and DA $\delta^{18}O_{speleothem}$. There is high coherence at 340-426 yr around 5500-5900 yr BP and at 96-128 yr around 7200-7500 yr BP.

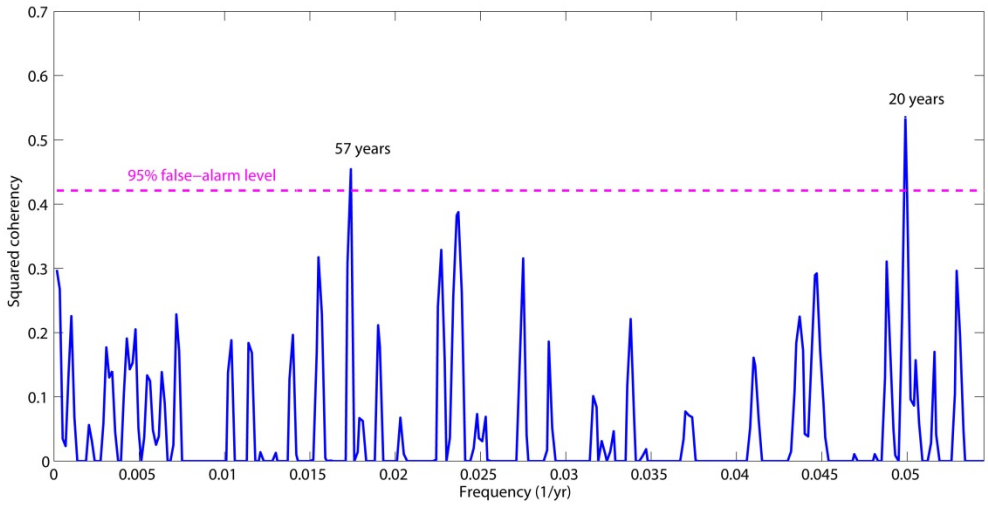

Figure 26. Coherency between atmospheric $\Delta^{14}C$ and DA $\delta^{18}O_{speleothem}$. The oversampling factor is 3, factor for highest frequency is 1 and false alarm level is 95% (dashed line). A Welch I window with 50% overlapping is employed to divide the signal into 8 segments in which linear trend of each segment is removed. At 57 yr and 20 yr, $\Delta^{14}C$ leads $\delta^{18}O$ values respectively by -109 degrees and 28 degrees.

References

Agnihotri, R., Dutta, K., Bhushan, R., and Somayajulu, B. L. K.: Evidence for solar forcing of the southwest monsoon during the last millennium, Earth Planet. Sci. Lett., 198, 521-527, 2002.

Araguás-Araguás, L., Froehlich, K., and Rozanski, K.: Stable isotope composition of precipitation over southeast Asia, J. Geophys. Res., 103(D22), 28, 721-28, 742, 1998.

Beer, J., Mende, W., and Stellmacher, R.: The role of the Sun in climate forcing, Quaternary Sci. Rev., 19, 403-415, 2000.

Bond, G., Kromer, B., Beer, J., Muscheler, R., Evans, M. N., Showers, W., Hoffmann, S., Lotti-Bond, R., Hajdas, I., and Bonani, G.: Persistent Solar Influence on North Atlantic Climate During the Holocene, Science, 294, 2130-2136, 2001.

Bradley, R. S.: Paleoclimatology: Reconstructing Climates of the Quaternary. Academic Press, San Diego, 1999.

Braun, H., Christl, M., Rahmstorf, S., Ganopolski, A., Mangini, A., Kubatzki, C., Roth, K., and Kromer, B.: Possible solar origin of the 1470-year glacial climate cycle demonstrated in a coupled model, Nature, 438, 208-211, 2005.

Burke, A., and Robinson, L. F.: The Southern Ocean's Role in Carbon Exchange During the Last Deglaciation, Science, 335(6068), 557-561, 2012.

Cai, Y., Tan, L., Cheng, H., An, Z., Edwards, R. L., Kelly, M. J., Kong, X., and Wang, X.: The variation of summer monsoon precipitation in central China since the last deglaciation, Earth Planet. Sci. Lett., 291, 21-31, 2010.

Clemens, S. C.: Millennial-band climate spectrum resolved and linked to centennial-scale solar cycles, Quaternary Sci. Rev., 24, 521-531, 2005.

Crowley, T. J.: Causes of climate change over the past 1000 years, Science, 289, 270-277, 2000.

Dykoski, C. A., Edwards, R. L., Cheng, H., Yuan, D., Cai, Y., Zhang, M., Lin, Y., Qing, J., An, Z., and Revenaugh, J.: A high-resolution, absolute-dated Holocene and deglacial Asian monsoon record from Dongge Cave, China, Earth Planet. Sci. Lett., 233, 71-86, 2005.

Fleitmann, D., Burns, S. J., Mudelsee, M., Neff, U., Kramers, J., Mangini, A., Matter, A.: Holocene forcing of the Indian monsoon recorded in a stalagmite from Southern Oman, Science, 300, 1737-1739, 2003.

Gimeno, L., de la Torre, L., Nieto, R., García, R., Hernández, E., and Ribera, P.: Changes in the relationship NAO–Northern hemisphere temperature due to solar activity, Earth Planet. Sci. Lett., 206, 15-20, 2003.

Gray, L. J., Beer, J., Geller, M., Haigh, J. D., Lockwood, M., Matthes, K., Cubasch, U., Fleitmann, D., Harrison, R. G., Hood, L., Luterbacher, J., Meehl, G. A., Shindell, D. T., van Geel, B., and White, W.: Solar Influences on Climate, Rev. Geophys., 48, 2010.

Grinsted, A., Moore, J. C., and Jevrejeva, S.: Application of the cross wavelet transform and wavelet coherence to geophysical time series, Nonlin. Processes Geophys., 11, 561-566, 2004.

Gupta, A. K., Das, M., and Anderson, D. M.: Solar influence on the Indian summer monsoon during the Holocene, Geophys. Res. Lett., 32, L17703, 2005.

Haam, E. and Huybers, P.: A test for the presence of covariance between time uncertain series of data with application to the Dongge Cave speleothem and atmospheric radiocarbon records, Paleoceanography, 25, PA2209, 2010.

Hahn, V. and Buchmann, N.: A new model for soil organic carbon turnover using bomb carbon, Global Biogeochem. Cy., 18, GB1019, 2004.

Haigh, J.: Climate variability and the influence of the sun, Science, 294, 2109-2111, 2001.

Higginson, M. J., Altabet, M. A., Wincze, L., Herbert, T. D., and Murray, D. W.: A solar (irradiance) trigger for millennial-scale abrupt changes in the southwest monsoon?, Paleoceanography, 19, PA3015, 2004.

Hong, Y. T., Wang, Z. G., Jiang, H. B., Lin, Q. H., Hong, B., Zhu, Y. X., Wang, Y., Xu, L. S., Leng, X. T., and Li, H. D.: A 6000-year record of changes in drought and precipitation in northeastern China based on a $\delta^{13}C$ time series from peat cellulose, Earth Planet. Sci. Lett., 185, 111-119, 2001.

Huang, N. E. and Shen S. S. P. (Eds.): Hilbert-Huang Transform and Its Applications. World Scientific., Singapore, 2005.

Huang, N. E. and Wu, Z.: A review on Hilbert-Huang transform: Method and its applications to geophysical studies, Rev. Geophys., 46, RG2006, 2008.

Hughen, K. A., Lehman, S. J., Southon, J., Overpeck, J. T., Marchal, O., Herring, C., and Turnbull, J.: ^{14}C Activity and Global Carbon Cycle Changes over the Past 50,000 Years, Science, 303, 202-207, 2004.

IPCC: Climate Change 2007: The Physical Science Basis, Contribution of Working Group I to the Fourth Assessment Report of the Intergovernmental Panel on Climate Change, edited by: Solomon, S., Qin, D., Manning, M., Chen, Z., Marquis, M., Averyt, K. B., Tignor, M., and Miller, H. L., Cambridge University Press, Cambridge, United Kingdom and New York, NY, USA, 996 pp., 2007.

Johnson, K. R. and Ingram, B. L.: Spatial and temporal variability in the stable isotope systematics of modern precipitation in China: implications for paleoclimate reconstructions, Earth Planet. Sci. Lett., 220, 365-377, 2004.

Jouzel, J., Hoffmann, G., Koster, R. D., and Masson, V.: Water isotopes in precipitation: Data/model comparison for present-day and past climates, Quaternary Sci. Rev., 19, 363-379, 2000.

Kitagawa, H. and van der Plicht, J.: Atmospheric radiocarbon calibration to 45,000 yr B.P.: Late glacial fluctuations and cosmogenic isotope production, Science, 279, 1187-1190, 1998.

Lachniet, M. S.: Climatic and environmental controls on speleothem oxygen isotope values, Quaternary Sci. Rev., 28, 412-432, 2009.

Legras, B., Mestre, O., Bard, E., and Yiou, P.: A critical look at solar-climate relationships from long temperature series, Clim. Past, 6, 745-758, 2010.

Marchitto, T. M., Lehman, S. J., Ortiz, J. D., Fluckiger, J., and Van Geen, A.: Marine Radiocarbon Evidence for the Mechanism of Deglacial Atmospheric CO_2 Rise, Science, 316, 1456-1459, 2007.

Mazaud, A., Laj, C., Bard, E., Arnold, M., and Tric, E.: Geomagnetic field control of ^{14}C production over the last 80 ky: Implications for the radiocarbon time-scale, Geophys. Res. Lett., 18(10), 1885-1888, 1991.

Muscheler, R., Beer, J., Wagner, G., and Finkel, R. C.: Changes in deep-water formation during the Younger Dryas event inferred from ^{10}Be and ^{14}C records, Nature, 408(6812), 567-570, 2000.

Muscheler, R., Joos, J., Beer, J., Muller, S., Vonmoos, M., and Snowball, I.: Solar activity during the last 1000 yr inferred from radionuclide records, Quaternary Sci. Rev., 26, 82-97, 2007.

Naegler, T. and Levin, I.: Biosphere-atmosphere gross carbon exchange flux and the $\delta^{13}CO_2$ and $\Delta^{14}CO_2$ disequilibria constrained by the biospheric excess radiocarbon inventory, J. Geophys. Res., 114, D17303, 2009.

Neff, U., Burns, S. J., Mangini, A., Mudelsee, M., Fleitmann, D., and Matter, A.: Strong coherence between solar variability and the monsoon in Oman between 9 and 6 kyr ago, Nature, 411, 290-293, 2001.

Rind, D.: The Sun's role in climate variations, Science, 296, 673-678, 2002.

Rose, K. A., Sikes, E. L., Guilderson, T. P., Shane, P., Hill, T. M., Zahn, R., and Spero, H. J.: Upper-ocean-to-atmosphere radiocarbon offsets imply fast deglacial carbon dioxide release, Nature, 466, 1093-1097, 2010.

Ruddiman, W. F.: Earth’s Climate: Past and Future. W. H. Freeman & Company, New York, 2007.

Schulz, M. and Stattegger, K.: SPECTRUM: Spectral analysis of unevenly spaced paleoclimatic time series, Comput. Geosci., 23, 929-945, 1997.

Shindell, D. T., Schmidt, G. A., Mann, M. E., Rind, D., and Waple, A.: Solar forcing of regional climate change during the Maunder Minimum, Science, 294, 2149-2152, 2001.

Skinner, L. C., Fallon, S., Waelbroeck, C., Barker, S., and Michel, E.: Ventilation of the deep southern ocean and deglacial CO_2 rise, Science, 328, 1147-1151, 2010.

Solanki, S. K., Usoskin, I. G., Kromer, B., Schüssler, M., and Beer, J.: Unusual activity of the Sun during recent decades compared to the previous 11,000 years, Nature, 431, 1084-1087, 2004.

Staubwasser, M., Sirocko, F., Grootes, P. M., and Segl, M.: Climate change at the 4.2 ka BP termination of the Indus valley civilization and Holocene south Asian monsoon variability, Geophys. Res. Lett., 30(8), 1425, 2003.

Steinhilber, F., Abreu, J. A., and Beer, J.: Solar modulation during the Holocene, Astrophys. Space Sci. Trans., 4, 1-6, 2008.

Steinhilber, F., Beer, J., and Fröhlich, C.: Total solar irradiance during the Holocene, Geophys. Res. Lett., 36, L19704, 2009.

Stocker, T. F. and Wright, D. G.: Rapid changes in ocean circulation and atmospheric radiocarbon, Paleoceanography, 11(6), 773-795, 1996.

Stuiver, M., Reimer, P. J., Bard, E., Beck, J. W., Burr, G. S., Hughen, K. A., Kromer, B., McCormac, G., van der Plicht, J., and Spurk, M.: INTCAL98 radiocarbon age calibration, 24,000-0 cal BP, Radiocarbon, 40, 1041-1083, 1998.

Suess, H. E.: Radiocarbon concentrations in modern wood, Science, 122, 415-417, 1955.

Torrence, C. and Compo, G. P.: A practical guide to wavelet analysis, Bull. Am. Meteorol. Soc., 79, 61-78, 1998.

Torrence, C. and Webster, P.: Interdecadal Changes in the ESNO-Monsoon System, J. Clim., 12, 2679-2690, 1999.

Wang, L., Sarnthein, M., Erlenkeuser, H., Grimalt, J., Grootes, P., Heilig, S., Ivanova, E., Kienast, M., Pelejero, C., and Pflaumann, U.: East Asian monsoon climate during the late Pleistocene: high-resolution sediment records from the South China Sea, Mar. Geol., 156, 245-284, 1999.

Wang, Y., Cheng, H., Edwards, R. L., He, Y., Kong, X., An, Z., Wu, J., Kelly, M. J., Dykoski, C. A., and Li, X.: The Holocene Asian monsoon: Links to solar changes and North Atlantic climate, Science, 308, 854-857, 2005.

Wu, Z. and Huang, N. E.: A study of the characteristics of white noise using the Empirical Mode Decomposition method, Proc. Roy. Soc. London Ser. A, 460, 1597-1611, 2004.

Wu, Z. and Huang N. E.: Ensemble Empirical Mode Decomposition: a noise-assisted data analysis method, COLA Technical Report 193, 2005.

Xiao, S. B., Li, A. C., Liu, J. P., Chen, M. H., Xie, Q., Jiang, F. Q., Li, T. G., Xiang, R., and Chen, Z.: Coherence between solar activity and the East Asian winter monsoon in the past 8000 years from Yangtze River-derived mud in the East China Sea, Palaeogeogr., Palaeoclimatol., 237, 293-304, 2006.

Yiou, P., Bard, E., Dandin, P., Legras, B., Naveau, P., Rust, H. W., Terray, L., and Vrac, M.: Statistical issues about solar-climate relations, Clim. Past, 6, 565-573, 2010.

Yuan, D., Cheng, H., Edwards, R. L., Dykoski, C. A., Kelly, M. J., Zhang, M., Qing, J., Lin, Y., Wang, Y., Wu, J., Dorale, J. A., An, Z., and Cai, Y.: Timing, duration and transitions of the last interglacial Asian monsoon, Science, 304, 575-578, 2004.

Zhang, P., Cheng, H., Edwards, R. L., Chen, F., Wang, Y., Yang, X., Liu, J., Tan, M., Wang, X., Liu, J., An, C., Dai, Z., Zhou, J., Zhang, D., Jia, J., Jin, L., and Johnson, K. R.: A test of climate, sun, and culture relationships from an 1810-year Chinese cave record, Science, 322, 940-942, 2008.